LES-RANS of installed ultra-high bypass-ratio coaxial jet aeroacoustics with flight stream

James C. Tyacke [*] , Zhong-Nan Wang [†] and Paul G. Tucker [‡]
Department of Engineering, University of Cambridge, Cambridge, UK

Using Large-Eddy Simulation-Reynolds-Averaged Navier-Stokes (LES-RANS), this paper studies a round coaxial nozzle with an ultra-high bypass-ratio of 15, with and without a wing-flap geometry. Depending on engine placement, the nozzle can become extremely close to the wing-flap geometry, introducing strong installation effects. Two different flap deflections of 8 and 14 degrees are contrasted with an isolated round nozzle. A flight stream is applied and an Ffowcs Williams-Hawkings (FWH) surface placement procedure for installed jets is proposed. Agreement with available experimental data is achieved for far-field overall sound pressure level and spectra as well as near field spectra. The LES provides a wider range of polar and azimuthal angles at 1 degree increments providing one of the most detailed acoustics data sets to date. The installed cases generate up to 20 dB more noise at mid-low frequencies due to large flap trailing edge sources. Additional sources are introduced by the interaction of the flight stream with the lifting surfaces. Second order space-time correlations reveal length and time scales in the flow. Fourth order space-time correlations indicate increasing magnitudes of the dominant noise source components with increasing flap angle. The 3D unsteady data set produced may lead to improved acoustics models.

Nomenclature

Acronyms/labels

Cell Number of cells

CFL Courant-Friedrichs-Lewy

Edge Number of edges

F08 8 degree flap angle

F14 14 degree flap angle

[*] Senior Research Associate, Department of Engineering, University of Cambridge, Cambridge, CB3 0DY, member AIAA.
[†] Research Associate, Department of Engineering, University of Cambridge, Cambridge, CB3 0DY, member AIAA.
[‡] Professor, Department of Engineering, University of Cambridge, Cambridge, CB3 0DY, Associate fellow AIAA.

FO Flyover

FS Flight stream

FWH Ffowcs Williams-Hawkings

Hex. Number of hexehedra

Inst. Installed

Iso. Isolated

LES Large-eddy simulation

OASPL Overall sound pressure level (dB)

Prm. Number of prisms

PS Pressure side

Pyr. Number of pyramids

RANS Reynolds-Averaged Navier-Stokes

SGS Sub-grid scale

SL Sideline

SPL Sound pressure level (dB)

SS Suction side

Tet. Number of tetrehedra

Greek

$'$ Fluctuation

β LES-RANS transition zone fraction

Δ Spatial increment (m), LES filter width (m)

δ Boundary layer thickness (m)

δ_{99} 99% freestream velocity boundary layer thickness (m)

δ_{ij} Kronecker delta

$\langle\,\rangle$ Time mean

μ Viscosity m^2/s

∇ Laplacian

- Spatial filter

ϕ Polar angle (degrees), flow variable

ρ Density (Kg/m^3)

τ Space-time time increment

τ_{ij} Modelled stress tensor

θ Azimuthal angle (degrees)

ε Smoothing parameter

Roman

u Cartesian velocity vector (m/s)

x Cartesian coordinate vector (m)

$\overline{L}$ Linear modelled stress

$\overline{NL}$ Nonlinear modelled stress

A Jacobian matrix

C_p Pressure coefficient

C_s Smagorinsky model constant

C_α Alpha model constant

D Bypass nozzle diameter (m)

d_{RANS} RANS layer extent (m)

d_{wall} Wall normal distance (m)

f Frequency (Hz), LES-RANS blending function

F_{ij} Edge flux

h	centreline to wing distance (m)
k	Turbulence kinetic energy (m^2/s^2)
P	Pressure (Pa)
R, r	Radius (m)
R_{ijkl}	Fourth order space-time correlation coefficient
R_{ij}	Second order space-time correlation coefficient
S_{ij}	Rate of strain tensor
St	Strouhal number
T	Temperature (K)
t	Time (s)
t^*	Non-dimensional time
Ti	Turbulence intensity

Sub/super-script

0	Total
a	Ambient
BP	Bypass
c	Core
i,j,k,l	coordinate indices
loc	Local
mean	Time mean
rms	Root mean squared

I. Introduction

The noise produced by aeroengines is a critical topic in engine design. The increase in air travel and tightening emissions targets require both airframe and aeroengine designers to accurately predict performance and pollutant and noise emissions. The Advisory Council for Aeronautical Research in Europe (ACARE) has set the target of a reduction in perceived noise emission of 50% (to those of the year 2000) by the year 2020. The EU Flightpath 2050 report states a 65% perceived noise level reduction relative to year 2000 levels as a goal [1]. The trend towards higher bypass ratio engines and closer integration with the airframe constantly changes the design space. This makes the use of simple correlations to predict noise less attractive if they are unable to capture the numerous effects on noise adequately. Viswanathan et al. [2] suggest there is a strong need to update existing methods. To enable such challenging targets to be met, the importance of the many influences on jet noise must be understood. Engine-airframe design is becoming more closely coupled, and Thomas [3], suggests a system level approach that includes propulsion airframe aeroacoustics is needed to reach noise reduction goals. Installation effects are therefore the main focus of this paper, where an isolated round nozzle is contrasted with an installed nozzle with two flap deflections.

Experiments have been used for decades to assess and improve designs, and build design tools for rather confined design spaces. They have also been used to reveal trends and noise sources using sophisticated data analysis, however the flow mechanisms responsible are still not fully understood. Viswanathan et al. [4] make space-time measurements of single stream hot and cold jets. They conclude that although peak pressure is found near the end of the potential core, low frequency coherent sources are found downstream of this. Bridges and Wernet [5] provide velocity spectra and second order correlations for cold and heated jets. Spectral characteristics and correlations were similar once the change in potential core length was accounted for. Fleury et al. [6] present space-time correlations of jets at two subsonic Mach numbers providing expressions for use in statistical models. Mengle et al. [7–9] systematically measure and study noise sources from a wide range of isolated and installed high bypass ratio round and serrated nozzles under flight conditions, but do not consider bypass ratios exceeding 7. Current designs are targeting bypass ratios of 15 and in future may reach 20. Brown [10] includes finite span effects of jet-flat-plate interaction into empirical models. Significant research has also been performed for future noise mitigation such as installed planar nozzles contrasted with round as Brown et al. [11]. Thomas et al. [12] study the overall effect of coaxial nozzle serrations, pylon, evelon deflection and application of acoustic liners. Mengle [13] also study the effect of reducing the gulley height and increasing flap angle between coaxial round and serrated jet nozzles under flight conditions, noting the appearance of two peaks in the installed spectra. Clearly much has been learned from experiments. However, experimental campaigns are expensive, and perhaps more importantly, may have time scales of months to years, surpassing design cycles. It can also be difficult to obtain 3D unsteady flow data, or reach certain operating conditions, for example to include flight stream effects without compromises in problem definition or additional corrections.

The multiple unsteady interactions for complex geometry jets make RANS unsuitable. Common linear RANS

models in their standard forms cannot accurately model a round jet plume (for example, the $k-\varepsilon$ model [14]), therefore, use for more complex installed jets does not appear feasible. Many models have been tested making use of various corrections for jet spreading rate, anisotropy, compressibility, heated jets, near wall effects and enhanced potential core mixing [15, 16]. These can be quite specific and inapplicable in the general case. For example, the nozzle could be serrated, eccentric, bevelled or could contain a lobed mixer. Georgiadis and DeBonis [17] provide a good overview of both RANS and LES modelling of jets. With the lack of a single reliable RANS model, there is a requirement to resolve the large scale eddies responsible for turbulence noise production.

Eddy resolving methods such as LES and hybrid LES-RANS are attractive to not only predict the flow and noise of jets, but to deeply analyse unsteady processes resulting in noise generation. Tam [18] notes, large coherent jet scales are large non-compact sources, indicating LES is ideal for revealing these. Freund [19] performs a low Reynolds number DNS of a single stream jet, calculating the Lighthill sound source. The radiating components were found not to coincide with turbulence kinetic energy, matching more closely with the full source, however the volume weighted contribution to the total noise matches relatively well. Bres [20] performs static hot and cold single stream LES at Reynolds numbers below 300,000, predicting far-field noise. Recently, DeBonis [21] studied the effects of temperature fluctuations for a single stream jet indicating a faster spreading rate, but relatively uniform Prandtl number. Xia et al. [22] use LES-RANS to study a single stream serrated nozzle, a coaxial jet with and without eccentricity and the independent effects of internal struts, pylon and wing-flap geometry. Vogel et al. [23] also study a coaxial jet (bypass ratio=5) with pylon and a single stream jet near ($1 < h/D < 3$) a flat plate. Source localisation is performed using beamforming identifying sources in the wake of the pylon, at the nozzle lip and plug. An increase in low frequency noise was observed for the installed cases. Lee et al. [24] study Lighthill source sub-terms and correlate these with far-field noise, indicating the interaction and contribution of these to far-field noise.

The FWH approach has been used with much success in conjunction with LES for the prediction of jet noise [25]. The use of a permeable FWH surface surrounding all noise sources avoids the expensive computation of volume source terms throughout the domain. For axi-symmetric domains, use of multiple FWH surfaces ensures the best surface placement [25, 26] (near the jet but far enough away from hydrodynamic effects). Nelson et al. [27] also provide some guidance on grid generation and FWH surface placement for an axi-symmetric single stream jet. A summary of our recent practice and validation is provided by Tyacke et al [28]. For complex geometries the optimum FWH surface placement is not clear *a priori*. Paliath and Premasuthan [29] use a simplified surface that encompasses the entire geometry a nearly uniform distance from the geometry. Another method is to base the FWH surface on an iso-surface of mean turbulence kinetic energy [30, 31]. The introduction of a flight stream compounds surface placement issues, strongly convecting vortices downstream, making FWH surface closure problematic. End disc averaging as [32] has been used with limited success but is not considered general enough [33]. Rahier et al. [34] use approximated quadrupole terms to effectively close the FWH surface reducing FWH placement and closure sensitivity. Pérez et al.

[35] attempt to filter the acoustic component from the near field. The inclusion of a flight stream will generate low frequencies downstream and hence requires a long FWH surface. This may adequately capture low polar angle noise without any special end disc treatment if other hydrodynamic regions are avoided near the control surfaces and jet plume.

The direct use of previous studies is limited in the high Reynolds number, installed, coaxial, hot jet noise context. Scattering of waves at the trailing edge, grazing of the wing by the jet, lift, wing sweep, flap angle, reflections, multiple shear layer refractions and flight stream effects make installed jet noise significantly more difficult to analyse as 3D fields lack symmetry or alignment with coordinate axes. Set in this backdrop, eddy resolving methods such as LES and hybrid LES-RANS are attractive to capture unsteady flow physics. Indeed, the methodology presented here, in combination with modelling of internal engine components as [36] goes a long way to meeting the system level aeroacoustics needs noted by Thomas [3]. The method should be quite general and applicable to a wide range of jets and perhaps landing gear. Here we focus on predicting far-field noise, noting areas of flow that require further source analysis. This is essentially a blind test, as data was available after the simulations were completed.

The paper is structured in the following way. The case setup and mesh are described. The numerical methods including the solver, turbulence modelling and acoustic processing are discussed. The results including flow, spectra, space-time correlations and acoustics are then presented and conclusions drawn.

II. Case setup

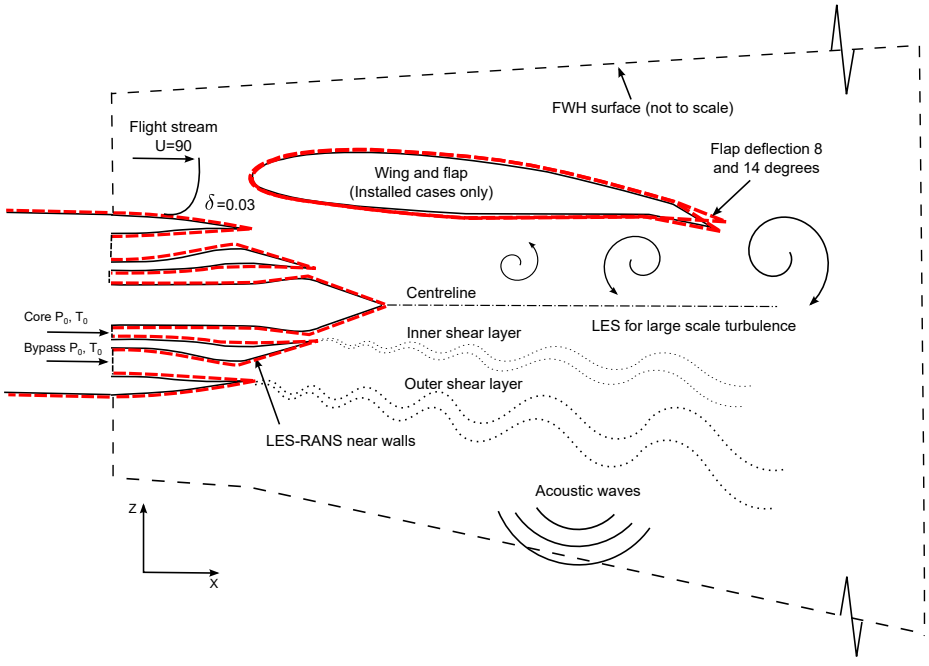

Fig. 1 Case setup schematic indicating boundary conditions and geometry features in the $y = 0$ plane.

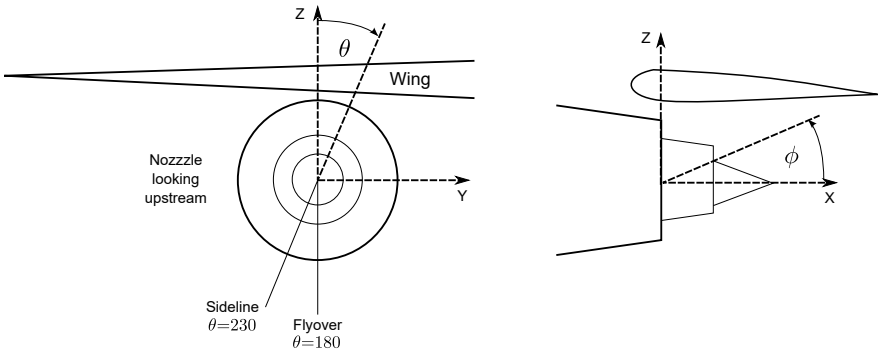

Fig. 2 Coordinate system showing azimuthal (left) and polar (right) coordinates.

Figure 1 indicates the main features of the geometry, modelling, flow and boundary conditions used. The bypass and core fluid stream inlets and the outer flight stream are indicated. Freestream conditions are applied at the flight stream inlet and radial far-field. Downstream, a subsonic outlet is used at atmospheric pressure. Near walls, as indicated by the red dashed lines, a RANS layer is used to model near wall streaks. Downstream LES is used to resolve large scale turbulent structures. The near field acoustic waves generated are recorded on the permeable FWH surface.

Table 1 Jet nozzle boundary conditions.

	Bypass	Core
P_0/P_a	1.342	1.222
T_0/T_a	1.128	2.652

Table 1 provides a summary of the nozzle conditions as indicated in Fig. 1. The boundary conditions for the isolated and installed cases are identical. At the bypass and core stream inlets, total pressure and total temperature conditions are imposed. P_a = 101325 Pa and T_a = 288.15 K. At the far field, ambient conditions and a flight stream of 90 ms^{-1} is set. The bypass nozzle diameter D = 0.228 m. The fully expanded velocities are u_c = 292 ms^{-1} and u_{BP} = 229 ms^{-1}. The isolated and installed nozzles are abbreviated as Iso. and Inst. respectively. The wing is tapered and swept, with the flap blended with the wing at each end. The installed flap deflections are denoted F08 and F14 for 8 and 14 degree flap deflections respectively. The flight stream is denoted FS followed by the flight stream velocity (m/s). The coordinate system used is shown in Fig. 2 along with the azimuthal locations of the sideline (SL) and flyover (FO) profiles.

III. Mesh

For all simulations, a hybrid structured-unstructured mesh is used. The mesh was generated using the ANSA pre-processor by Beta-CAE. A structured hexahedral mesh is utilised in the jet plume region. This is less dissipative and fills volumes efficiently. Outside of the jet plume, unstructured tetrahedral mesh is used. This can be seen in Fig. 3(a). This allows the complex wing-flap geometry to be embedded easily and provides mesh consistency between simulations. Figure 3(a) also contains an inset showing the structured-unstructured interface. At the interface the ratio

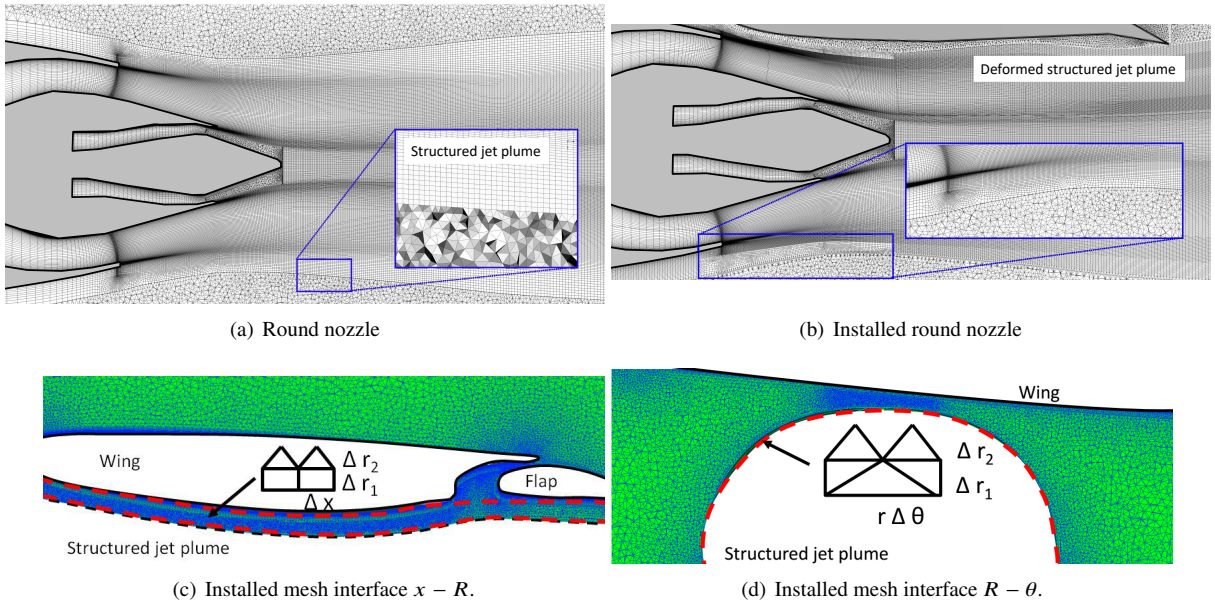

(a) Round nozzle

(b) Installed round nozzle

(c) Installed mesh interface $x - R$.

(d) Installed mesh interface $R - \theta$.

Fig. 3 Hybrid structured-unstructured mesh for (a), an isolated nozzle and (b), an initial installed round coaxial nozzle, (c), structured-unstructured interface in the $x - R$ plane,(d), structured-unstructured interface in the $R - \theta$ plane.

of Δx and $R\Delta\theta$ is kept below 2 [37]. A small degree of radial stretching also allows ΔR to be relatively well matched. As the number of azimuthal and radial nodes are fixed, the interface relies on the axial distribution. In all meshes the axial expansion ratio is kept between $0.5 - 1.0\%$. Near the nozzle, a 2-dimensional $(x - R)$ quad-dominant mesh is used (inset in Fig. 3(c)) to prevent fine axial mesh radiating outwards and reconciles the interface radial location which lies within the nozzle for small mesh spacings. This mesh is extruded circumferentially with a uniform spacing giving a total of $160\Delta\theta$. As shown in Fig. 3(b), for installed cases, the jet plume is deformed to follow the shear layer trajectories under the wing-flap. This is done following a short run on a preliminary mesh. The wing and flap geometries are surface-meshed using 2D structured and quad-dominant unstructured mesh. Layers are then extruded in the wall normal direction. The quad dominant surface mesh gives hexahedral prism cells predominantly aligned with the mean flow in boundary layer regions. To avoid jumps in mesh resolution at interfaces between the prism layers and the outer tetrahedral mesh, the surface mesh resolution is chosen based on the growth rate and number of layers so that the final wall normal spacing matches the surface mesh spacing within a factor of two giving a reasonably isotropic cell aspect ratio. An additional restriction is to match the outer mesh spacing of the structured jet plume mesh with the surface mesh requirements of the wing-flap prism layers. The mesh near the nozzle is of a similar scale in the x and R directions. A gap of approximately 8-10 average mesh spacings was left between the deformed structured mesh and the outer wing-flap layers to allow a smooth transition. This is indicated in in Fig. 3(c) by the dashed region. As the tetrahedral cells are isotropic, to match the $R\Delta\theta$ spacing, the number of θ points was locally doubled in the upper plume interface so that the $R\Delta\theta \approx \Delta R \approx \Delta x$. This is indicated in Fig. 3(d) by the dashed line. Based on expected frequencies

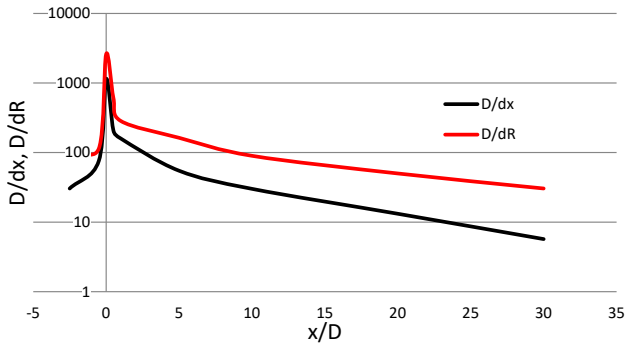

Fig. 4 Mesh distribution along the outer shear layer lip-line for the F14 case at $\theta = 0$.

at different axial and radial locations, a nest of cylindrical volumes were used to limit maximum mesh spacing and expansion ratio of $1.05 - 1.06$ up to the last FWH surfaces where the expansion ratio was then relaxed to 1.2 for the sponge region. The overall mesh statistics are presented in Tab. 2. We have previously established with our current numerical scheme that approximately 10 points per eddy provides adequate resolution [28, 38]. The smallest scales at the nozzle lip (0.005D) and largest scales downstream OD, provide bounding guidelines, which with low mesh expansion, provide well resolved turbulence within this range. The main loops in the solver scale with N_{edge} which indicates relative computation effort. The approximate mesh distribution for the installed F14 case is shown in Fig. 4.

Table 2 Mesh statistics ($N \times 10^6$).

	N_{node}	$N_{Hex.}$	$N_{Tet.}$	$N_{Pyr.}$	$N_{Prm.}$	N_{cell}	N_{edge}
Iso.	32	29	16.8	0.22	0.032	46.2	107.6
F08	58.6	42.2	75.2	1.11	5.83	124.4	229.5
F14	62.4	44.4	78.4	1.24	7.80	131.8	244.1

Using these meshes, computational resources are provided in Tab. 3 where a convective time unit $t^* = D/u_{BP}$. To develop the flow, and remove low frequency transients, a diminishing physical time step corresponding to $4 \geq CFL \geq 1$ (based on axial grid spacing and bulk velocity at the nozzle exit) is used. In Tab. 3 an equivalent number of development t^* to using the final time step is given. The physical t^* for flow development are given in brackets. A rate of \$0.05/ core hour is used to obtain the total cost. Clearly, a measure of statistical stationarity is required to minimise both development and data collection run times. In the current work, manual inspection of statistics was carried out between runs. This could be automated in future to minimise cost.

Table 3 Costs of simulations.

	t^* to develop	t^* data collection	Total core hours (10^6)	Approximate cost (k)
Iso.	150 (275)	160	0.6	\$ 20.4
F08	150 (275)	200	1.5	\$ 51.4
F14	150 (275)	220	1.8	\$ 60.2

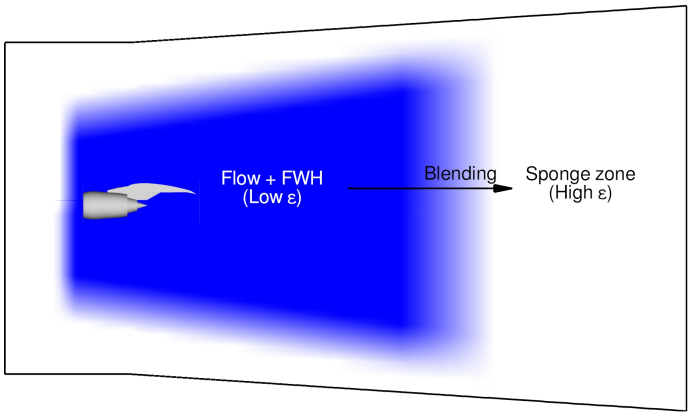

Fig. 5 Numerical smoothing applied in the computational domain (not to scale).

IV. Numerical Methods

A. Solver

An unstructured finite volume, edge-based compressible solver is used. Second order backward differencing is used for time and a second order kinetic energy preserving (KEP) discretisation [39] is used in space with numerical smoothing adapted for jet simulations. The solver is proprietary but has been extensively validated [28, 33, 36, 40, 41]. The KEP cell face flux with additional numerical smoothing is given by equation (1). Previous tests using homogeneous decaying turbulence with hexahedral, tetrahedral and prism elements showed the KEP scheme was less sensitive to cell type than the previous Roe scheme. This enables the use of the hybrid meshing strategy presented.

$$F_{ij} = \frac{1}{2}\left(\rho_i + \rho_j\right) \times \frac{1}{2}\left(u_i + u_j\right) \times \frac{1}{2}\left(\phi_i + \phi_j\right) - \frac{1}{2}\varepsilon|A|[\nabla_i^2\phi - \nabla_j^2\phi] \tag{1}$$

The parameter ε is used to minimise numerical dissipation in the central jet flow and FWH region and is increased along with mesh expansion to form sponge zones near the far-field boundaries preventing wave reflections. This is shown in Fig. 5.

B. Turbulence modelling

To alleviate near wall grid requirements, a hybrid LES-RANS model is used. LES-RANS has been used with success for jets and other complex flows [28, 33, 36, 42, 43]. Near walls, the Spalart-Allmaras RANS model [44] is used to model the inner boundary layer. Outside of the RANS layer where larger scales dominate, a mixed non-linear alpha LES model is used [45] to resolve complex unsteady flow features. The Smagorinsky SGS model [46] is used to provide dissipation with a constant of $C_s = 0.1$ and the alpha model is used to add non-linear terms, modelling anisotropic regions. Upstream of the potential core, the SGS filter is defined as $\Delta_{SGS} = (\Delta_x\Delta_y\Delta_z)^{(1/3)}$ to appropriately capture shear layer development. After the end of the potential core ($x/D \approx 10$), $\Delta_{SGS} = max(\Delta_{max}, (\Delta_x\Delta_y\Delta_z)^{(1/3)})$

in order to suitably model the more isotropic flow structures on the anisotropic mesh downstream. To provide a smooth transition from the RANS to LES, a function is used to blend the two models. The overall model is described by Equations 2-4.

$$\tau_{ij}^{model} = \overline{L} + \overline{NL} \tag{2}$$

$$\overline{L} = \frac{\tau_{kk}\delta_{ij}}{3} + 2[f \cdot \mu_{SGS} + (1-f) \cdot \mu_{RANS}]S_{ij} \tag{3}$$

$$\overline{NL} = \rho C_{\alpha} \Delta_{SGS}^2 f(\frac{\partial u_i}{\partial x_l}\frac{\partial u_l}{\partial u_j} + \frac{\partial u_i}{\partial x_l}\frac{\partial u_j}{\partial u_l} + \frac{\partial u_l}{\partial x_i}\frac{\partial u_l}{\partial u_j}) \tag{4}$$

$S_{ij} = 0.5(\partial u_i/\partial x_j + \partial u_j/\partial x_i)$ is the strain rate tensor and the blending function is given as

$$f = min[max(\frac{d_{wall} - (1-\beta)d_{RANS}}{\beta d_{RANS}}, 0), 1] \tag{5}$$

where d_{RANS} is the RANS layer thickness and β defines the size of the RANS to LES transition zone as a fraction of d_{RANS}. To account for different fluid stream velocities, d_{RANS} is set locally. The boundary layer for the nacelle was specified as $\Delta_{99} = 30$ mm. The RANS layer was thickened to 35 mm to ensure this. The flap and wing underside interact with the jet, and the flap also receives resolved turbulence from the wing cove. Therefore a RANS layer was used until $y^+ = 200$. A RANS layer thickness of $y^+ = 1000$ was applied on the interior nozzle surfaces as no boundary layer data was provided by measurements or otherwise specified. The boundary layer profile is considered of secondary importance to the dominance of the intense shear layer at the nozzle lip. The RANS layer also prevents separation on the plug as Eastwood et al. [40].

C. Acoustics processing

A permeable FWH surface is used to record time series of the primitive variables for later processing using an FWH solver. The use of multiple FWH surfaces has proven to be useful in ensuring only acoustic signals are being recorded at the surface and not vortical/hydrodynamic signals. The ideal placement of FWH surfaces is challenging *a priori*, hence the use of multiple surfaces allows data to be recorded and assessed later. Defining an FWH surface for an installed jet is challenging in itself. The addition of a flight stream however introduces strong wing-flap interaction with jet plume deflection and shed vortices that travel far downstream. It was decided to use conservative geometry and flow based criteria to determine the surfaces used. Three criteria were defined based on wall distance, turbulence intensity and non-dimensional vorticity. These are $d_{wall} > 0.25D$, $Ti < 0.25\%$ and $|\Omega|D/u_{BP} < 0.05$ respectively as [31]. Ti provides an indication of the Lighthill stress tensor (at high Reynolds number and with a low temperature difference

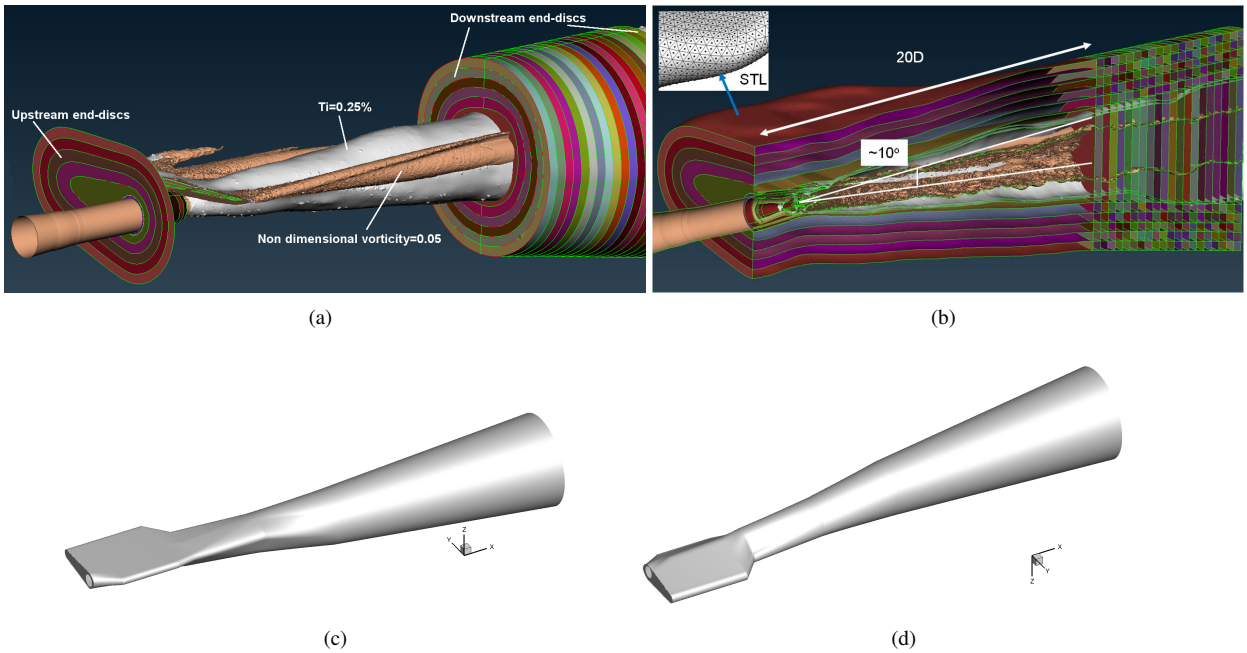

(a) (b)

(c) (d)

Fig. 6 FWH surface placement.

between the jet and ambient flow). Vorticity indicates where hydrodynamic fluctuations occur that we wish to avoid. We do not want to cut through geometry such as the wing due to flow unsteadiness (such as unsteady lift) that could contaminate FWH data. The two flow criteria are indicated in Fig. 6(a). The outermost of any of these surfaces was chosen to define a complex 3D surface extending throughout the domain in the upstream and downstream directions. This was then offset in the surface normal direction several times as shown in Fig. 6(b). End-disc filtering has been tested previously [33] but is not a general approach. Development of the jet depends on the jet operating condition and flight stream velocity. These set a single assumed frequency and end-disc spacing for filtering, whereas jets are broadband in nature. Multiple closing discs with different axial and radial limits were however also created as shown in the previous figures. Hence data is recorded for numerous scenarios and further processing. The innermost surfaces used are shown in more detail in Figs. 6(c)-6(d) looking from above and below the wing respectively. The surrounded nozzle, wing, tip vortices and eventual jet plume return to roundness is visible. Results presented use upstream closing surfaces to capture installation noise at high polar angles. The downstream end is left open, but a sufficiently long surface ensures sound sources are captured at low polar angles. The current method for generating a long, open surface, should be general and could be used for other challenging applications such as landing gear noise.

The convective formulation of the FWH equation of [47] is used to project the near field source to the far-field. Far-field sound is calculated at 3, 6 and 12 m using the FWH method in accord with the expected microphone locations in the experiments. Results are presented for 6m where current measurements are available. The LES and measured data do not show a significant difference between the 3 radii when back propagated to an emission distance of 1 m.

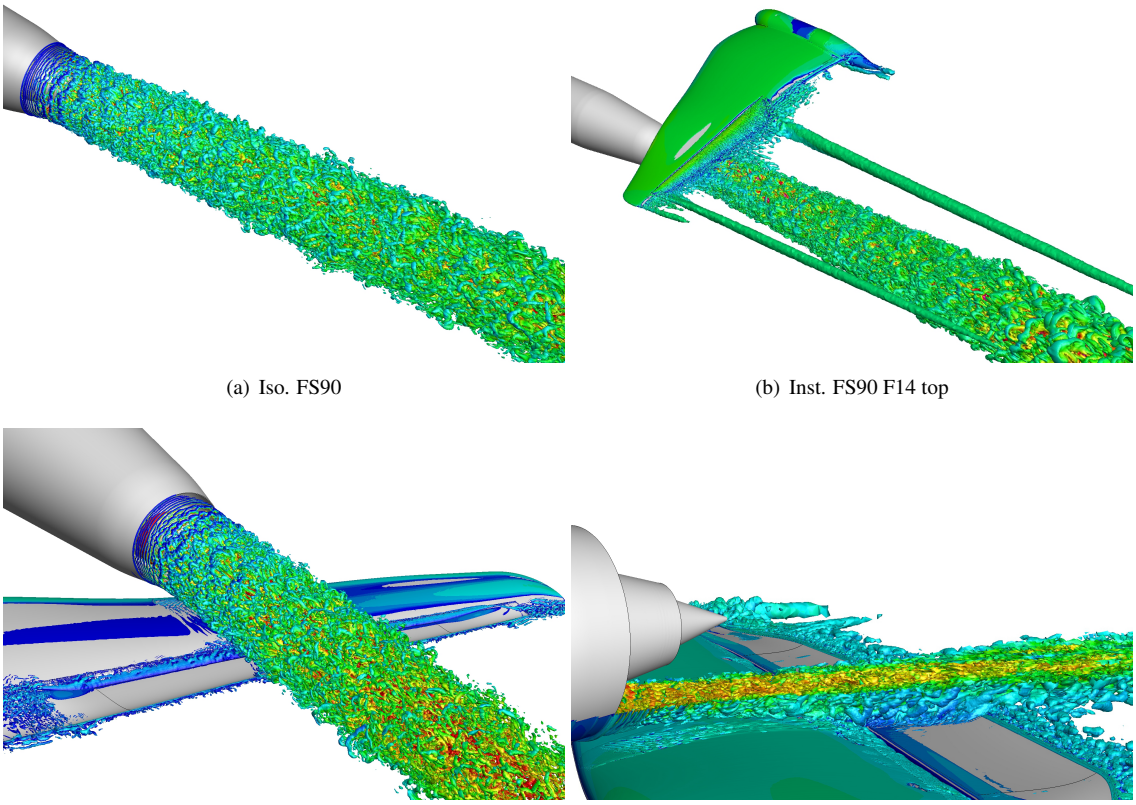

(a) Iso. FS90

(b) Inst. FS90 F14 top

(c) Inst. FS90 F14 bottom view 1

(d) Inst. FS90 F14 bottom view 2 (region above flap blanked)

Fig. 7 Q-criterion coloured by axial velocity for the Iso. and F14 cases.

High- and low-pass filters were used when integrating spectra to obtain the OASPL so that under-resolved low and high frequencies can be removed and a consistent frequency range compared. The same filtering was applied to the pressure time series to calculate the equivalent OASPL using p_{rms} and the OASPL was nearly identical to the integral of each spectrum. We have hence provided data where we believe we are resolved in the range $80 < f < 3000$ Hz and beyond. For sound pressure levels, corrections for reception to emission angle and back propagation to a distance of 1 m are applied.

V. Results

A. Instantaneous and Mean Flow

Figure 7 shows Q-criterion isosurfaces for both isolated and F14 cases. The installed cases generate a complex flow and the flight stream convects vorticity from the jet, flap and wing tip far downstream. Turbulence from the outer shear layer is ingested into the flap recess. Above the jet, fluid separates from the wing PS recess corner before being ingested into the recess, accelerated and generating turbulence along the length of flap suction side. Figure 7(d) shows perturbations from the shear layer triggering small velocity fluctuations on the wing PS from $x/D = 0.125$.

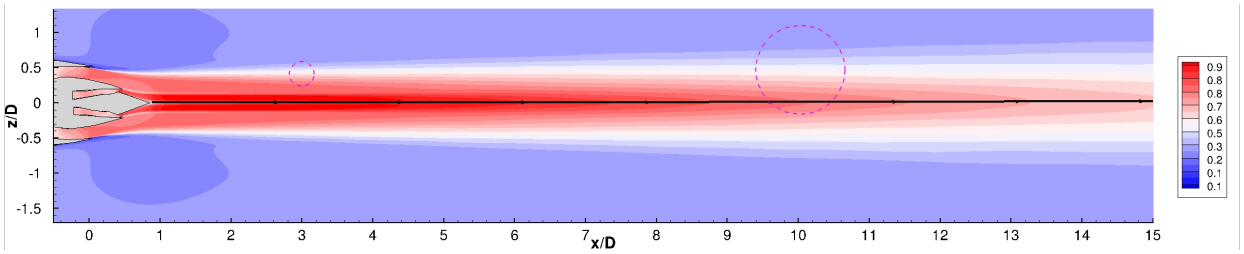

(a) Iso.

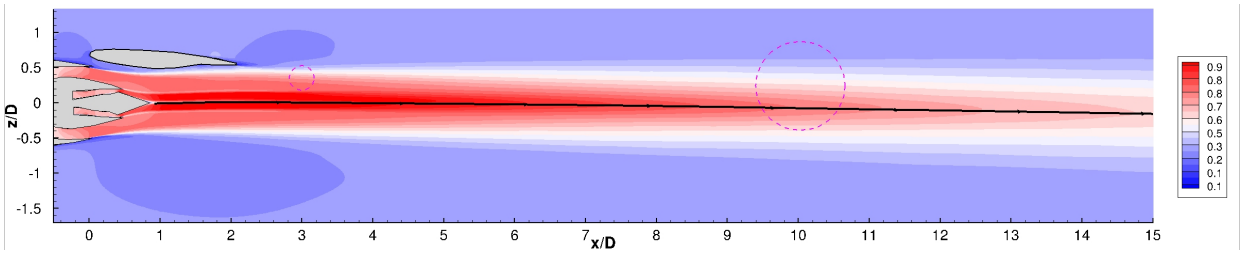

(b) Inst. F08

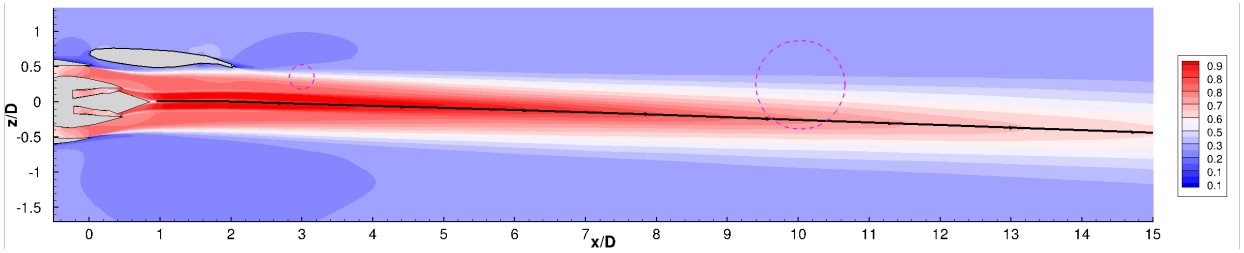

(c) Inst. F14

Fig. 8 Axial velocity contours ($\langle u \rangle / u_c$) for the isolated and installed cases at the $y = 0$ plane. Streamlines are indicated to provide an equivalent centreline profile.

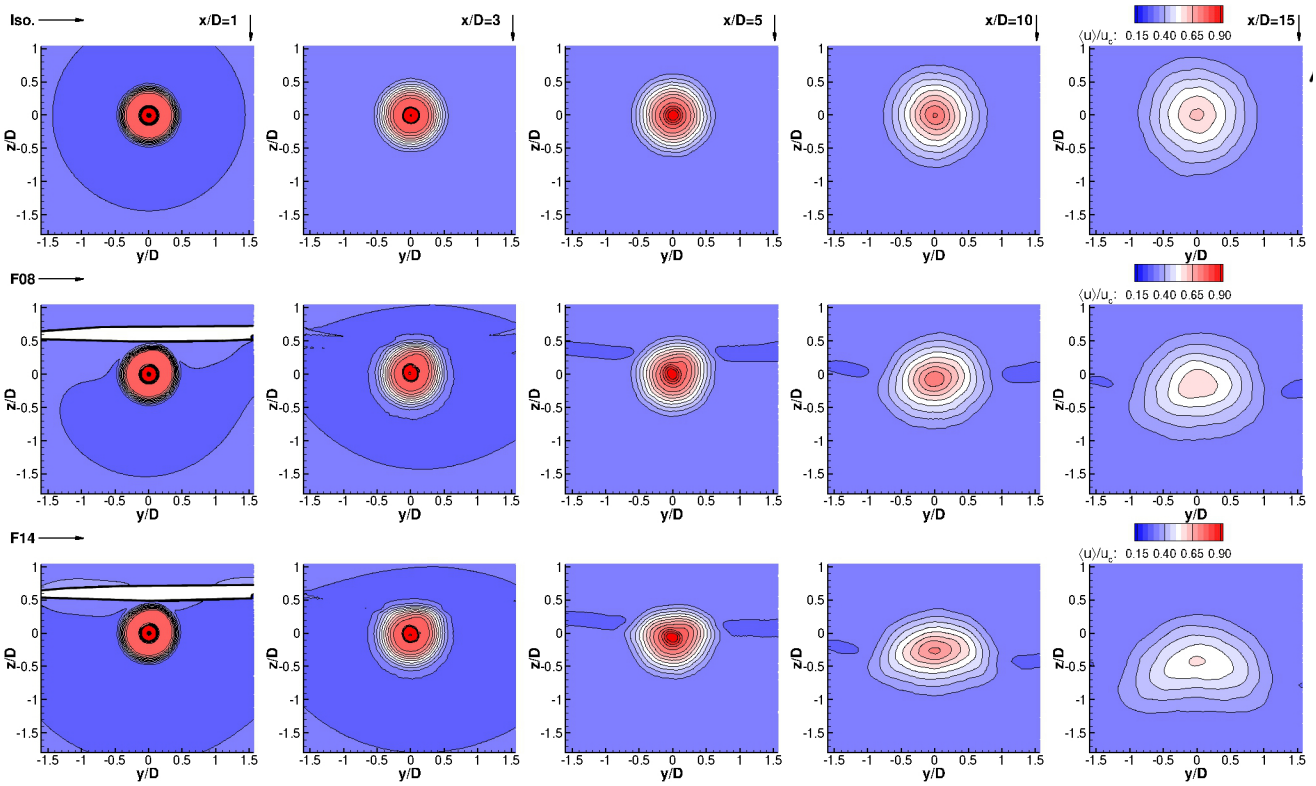

Fig. 9 Axial velocity contours ($\langle u \rangle / u_c$) at different $x-$planes. Rows represent cases, columns represent axial plane locations as labelled.

Figure 8 shows axial velocity contours in the $y = 0$ plane for the cases studied. Also indicated is an equivalent centreline for each case by a black stream line and the space-time probe locations (dashed circles) discussed in Section E. For the F08 case, the effect on jet plume deflection is minimal, indicating the case may be used to contrast the presence of surfaces near the nozzle and more dramatic modification of the jet plume as with the F14 case. The F14 case shows the jet plume initially deflected towards the wing, then downwards by around $0.5D$ at $x/D = 15$. The plume deflection angle based on the provided streamline extremities is approximately 0 and 2 degrees for the F08 and F14 cases respectively.

Figure 9 shows the mean axial velocity development downstream of the nozzle for each case. At $x/D = 1$ under the wing, the jet is not deformed significantly. Downstream of the flap at $3 < x/D < 5$ the jet plume deforms, increasing with flap angle. Vortices generated by the spanwise extremities of the flap and penetration of the flap into the edge of jet further deform the plume at $\theta = 90^o$ (positive y) and $\theta = 270^o$ (negative y) eventually causing the plume to form a kidney shape in the region $10 < x/D < 15$.

B. Velocity, pressure and temperature fluctuations

1. Turbulence kinetic energy

Figure 10 shows turbulence kinetic energy contours in the $y = 0$ plane. For all cases the inner shear layer transitions reaching a mid-value of $\langle k \rangle / u_c^2 = 0.005$ at $x/D = 2.5$. Due to the relatively low velocity ratio of the core and bypass streams, little shear is generated. The outer shear layer then dominates, although is not as intense as for static jets due to the flight stream. The outer and inner shear layers merge at approximately $x/D = 11$ for the isolated case (Fig. 10(a)). For the installed cases, the outer shear layer mixing is intensified in the upper region by the flap, and is further deflected downwards with increasing flap angle. For the F14 (and the a lesser extend the F08) case, $\langle k \rangle$ remains high in the upper shear layer and penetrates to the jet plume centre at $x/D = 10$. At $x/D = 1$, the presence of the wing also suppresses peak $\langle k \rangle$ by 25% relative to the Iso. case. This suppression of turbulence promotes a rapid growth downstream of the flap, where turbulence from the flap SS mixes intensely with the jet shear layer from the flap PS. This production of $\langle k \rangle$ is greater with increased flap angle. Downstream of the flap, peak $\langle k \rangle$ occurs at $x/D = 2.77$ ($\langle k \rangle / u_c^2 = 0.014$) for the F14 case, and $x/D = 3.05$ ($\langle k \rangle / u_c^2 = 0.012$) for the F08 case, equating to around a 15% increase and $0.3D$ shift upstream between the F08 and F14 cases.

Turbulence intensity $\langle k_{loc} \rangle^{\frac{1}{2}} / u_{loc}$ is shown near the flap in Fig. 11 for the F14 and F08 cases. For the F14 case, the turbulence intensity reaches values above 50% in the flap recess, at the flap leading and trailing edges and along the flap SS at greater than half the chord axially. For the F08 case Ti at the leading edge is reduced.

Figure 12 shows the development of k axially for each case. At $x/D = 3$, downstream of the flap, with increasing flap deflection, the upper, outer shear layer becomes more broad, flat and intense at $z/D \approx 0.5$. This trend continues downstream, $\langle k \rangle$ showing a similar shape to $\langle u \rangle$ (Fig. 9). Overall the F14 case develops higher $\langle k \rangle$ especially in the

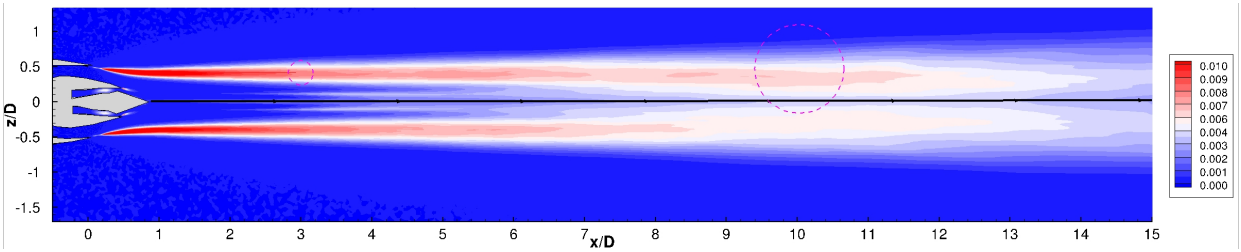

(a) Iso.

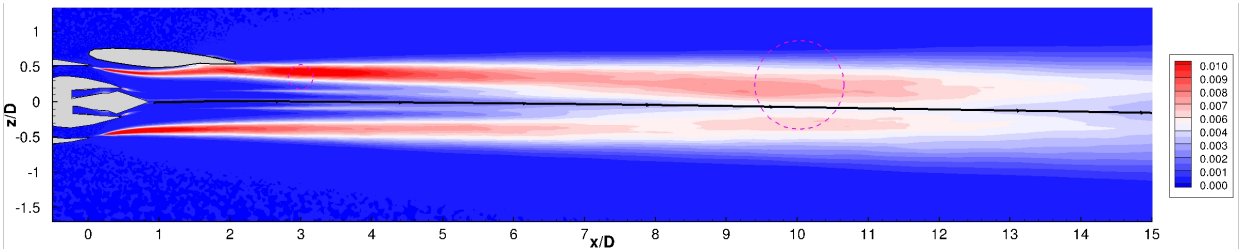

(b) Inst. F08

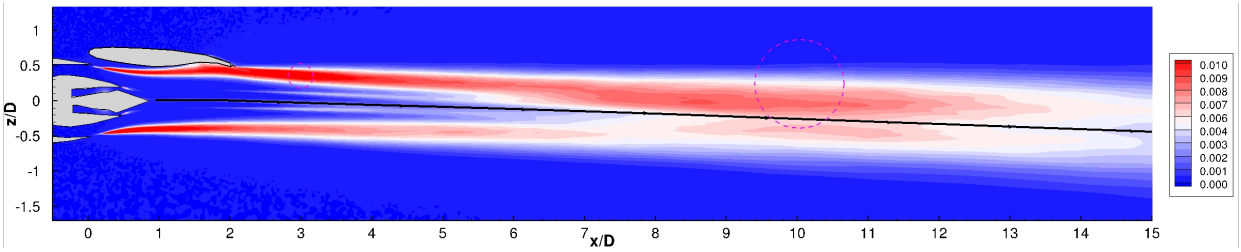

(c) Inst. F14

Fig. 10 Turbulence kinetic energy contours ($\langle k \rangle / u_c^2$) for the isolated and installed cases at the $y = 0$ plane.

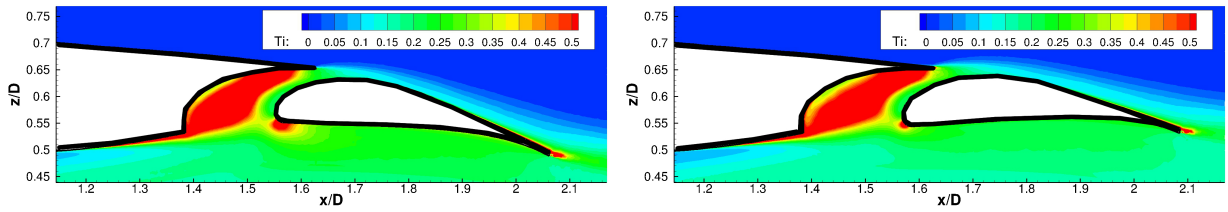

(a) F14 (b) F08

Fig. 11 Turbulence intensity (T_i) contours near the flap for installed cases F14 and F08 ($y = 0$ plane).

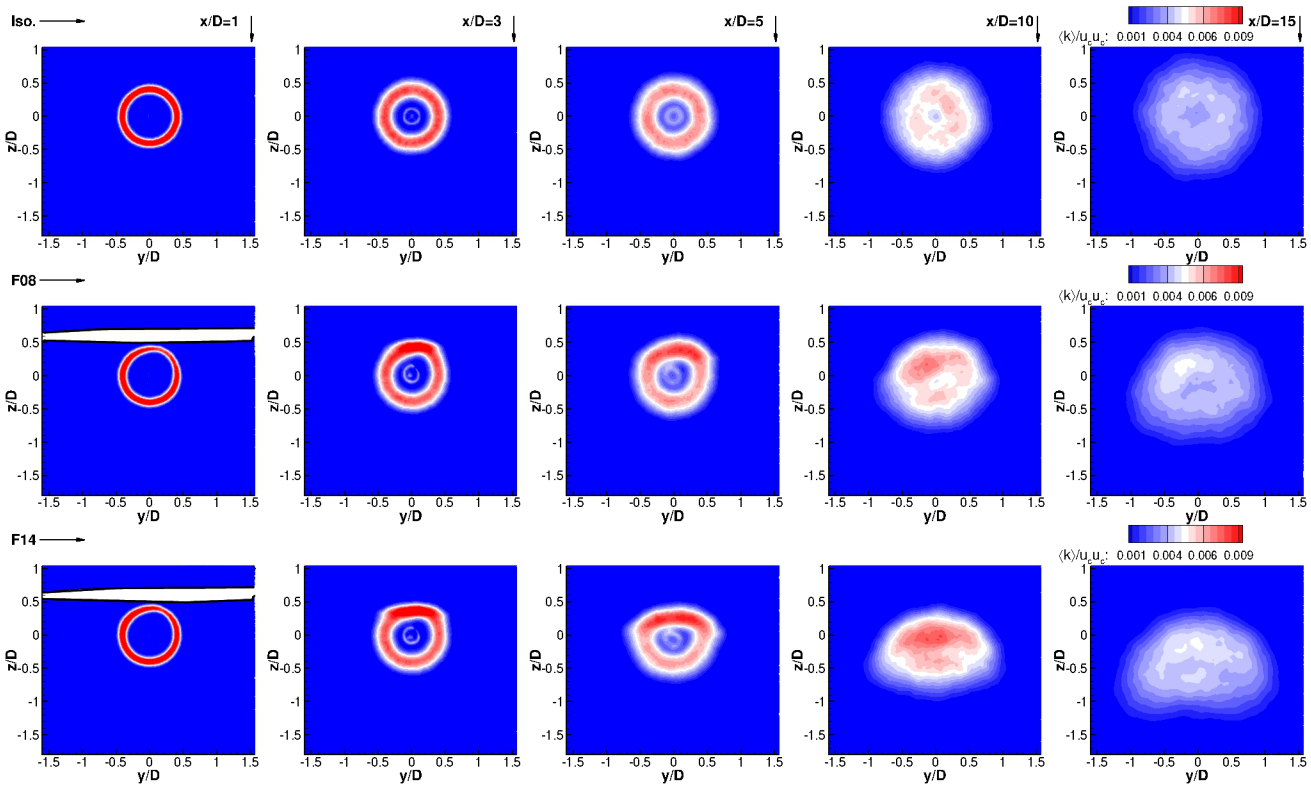

Fig. 12 Turbulence kinetic energy contours ($\langle k \rangle / u_c^2$) at different $x-$planes. Rows represent cases, columns represent axial plane locations as labelled.

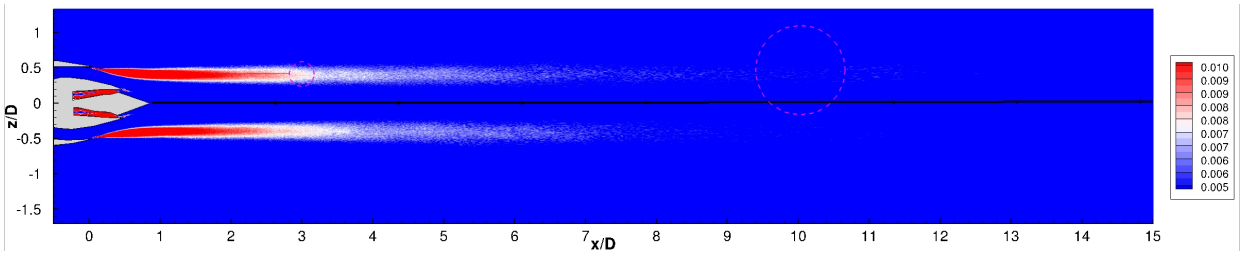

(a) Iso.

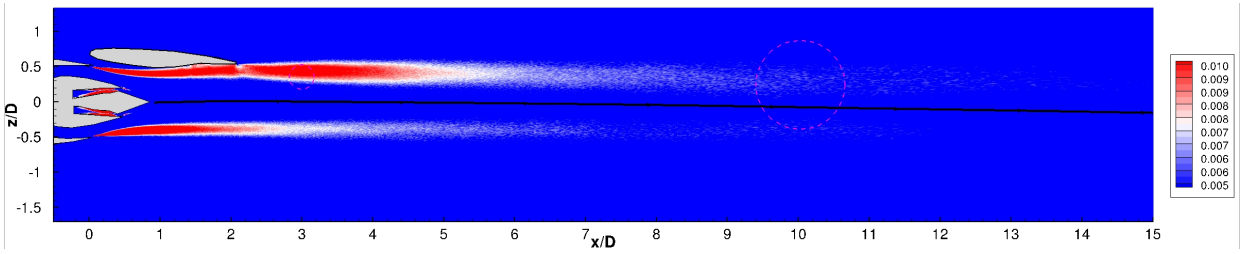

(b) Inst. F08

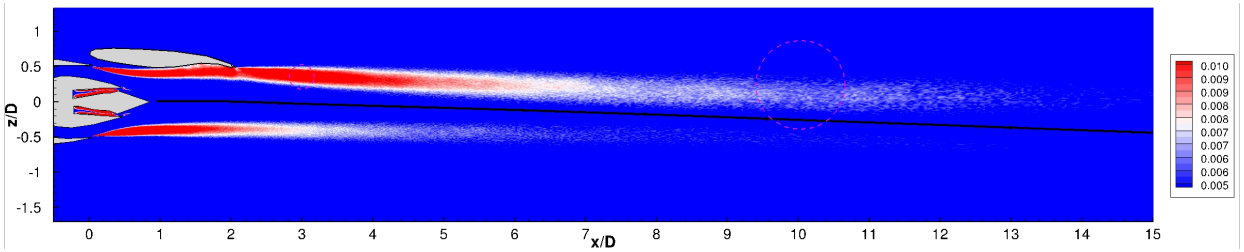

(c) Inst. F14

Fig. 13 Static p_{rms} contours ($\langle p' \rangle / p_a$) for the isolated and installed cases at the $y = 0$ plane.

upper outer shear layer indicating a greater potential noise source over a large axial region.

2. Pressure and temperature fluctuations

Figure 13 shows p_{rms} contours. The F08 case displays higher p_{rms} values downstream of the wing-flap to the Iso. case. The F14 case further intensifies the pressure fluctuations downstream of the wing-flap, which then decay slowly and extend further downstream. In contrast to the $\langle k \rangle$ contours, the most intense pressure fluctuations remain within $6 < x/D < 7$ in the wake of the wing-flap.

Figure 14 shows static T_{rms} contours for the F14 case. Comparison with the isolated and F08 case shows no significant difference. This is expected as there is little mixing of the core and bypass streams until $x/D > 3$. The UHBPR nozzle generally acts similarly to a single stream cold jet and noise is expected to be dominated by the outer shear layer.

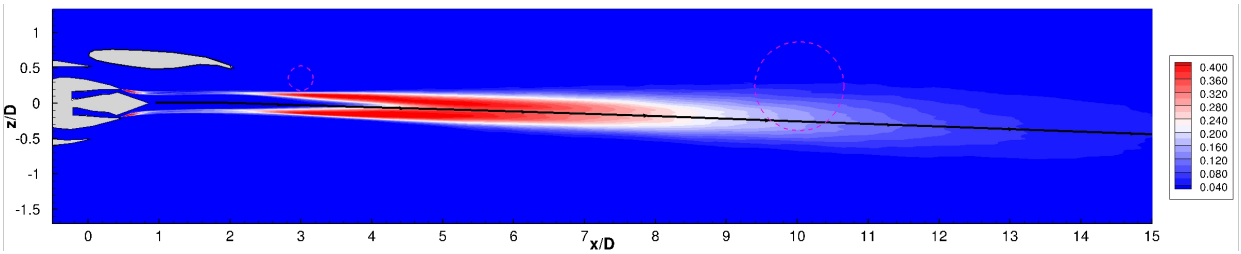

Fig. 14 Static T_{rms} contours ($\langle T' \rangle / T_a$) for the F14 case at the $y = 0$ plane.

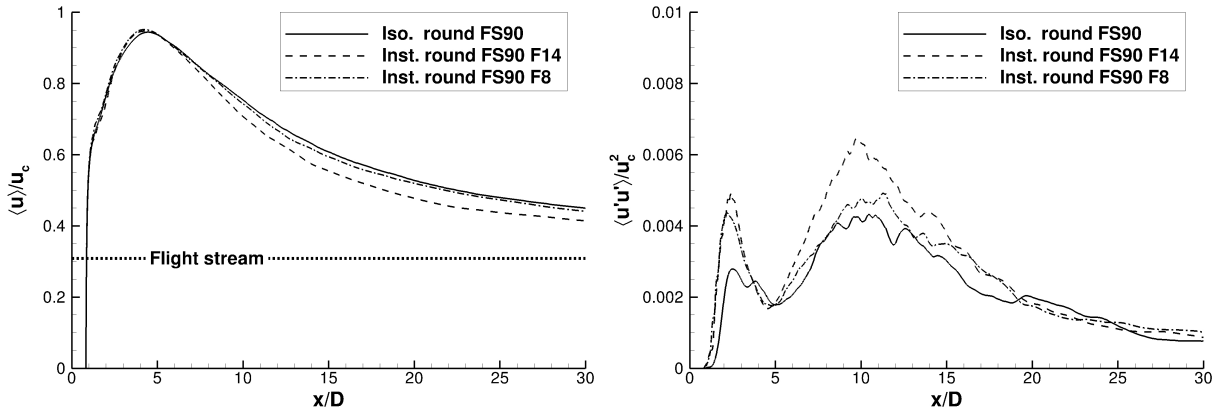

(a) Axial velocity (b) Axial Reynolds stress

Fig. 15 Axial velocity and Reynolds stress profiles along a streamline from the plug centre.

C. Velocity and turbulence profiles

1. Radial profiles

Figure 15(a) displays the axial velocity development along the a streamline starting at the plug centre (equivalent to the isolated jet centreline). These are indicated in Fig. 8 by black streamlines. For the isolated case, downstream of the plug, the velocity rises rapidly before a more gradual rise as density variations due to hot core flow and mixing of the bypass flow produce a peak at $x/D = 5$. There is then a slow decay as a result of the flight stream. This is in contrast to single stream hot jets without flight stream, which begin with the maximum velocity and decay rapidly. The isolated profile is modified by the wing and flap. The downstream decay of the F08 case is similar to the isolated case. The F14 decay is faster, reaching $\langle u \rangle / u_c = 0.5$ around $5D$ further upstream than the F08 case. Figure 15(b) shows peaks in the axial Reynolds stresses. The first peak is due to the plug wake. The axial Reynolds stresses of F08 and F14 cases are increased by approximately 50-75% relative to the isolated case at $x/D = 2.5$. This is in the vicinity of the flap trailing edge for the installed cases ($x/D \approx 2.1$ at the flap centre). The installed cases generate higher activity in the plug wake. This is attributed to additional disturbances introduced throughout the jet plume. The second, broader peak in Fig. 15(b), corresponds to the final merging of the shear layers into a single plume, akin to the end of the potential core of a single stream jet. Fig. 16 shows between $2.5 < x/D < 3.5$, the inner shear layer begins to merge with the

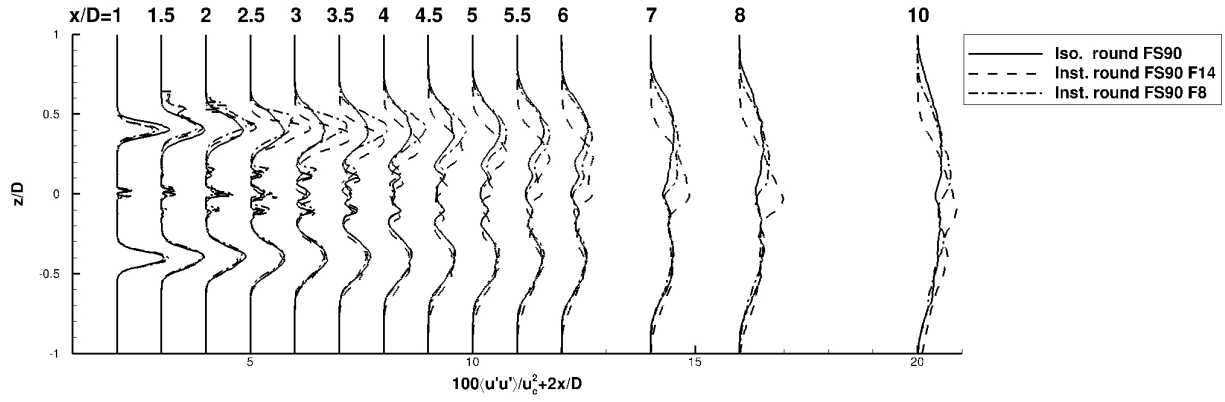

(a) $y = 0$ plane

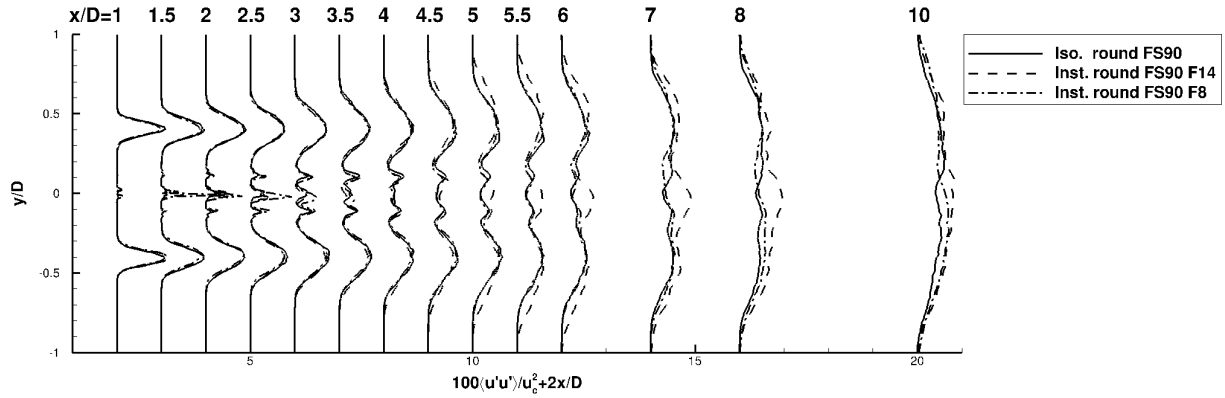

(b) $z = 0$ plane

Fig. 16 Reynolds axial stress profiles at $y = 0$ and $z = 0$ planes.

plug wake and the outer shear layer. For coaxial nozzles, mixing occurs over a larger region, as energy is drained from different fluid streams. The peak location and turbulence level for the isolated and F08 cases are similar. The F14 case again increases the peak Reynolds stress by 50% and creates a sharper peak at $x/D = 10$. After $x/D = 20$, levels are similar for all cases.

Figure 16 shows axial Reynolds stress profiles at $y = 0$ and $z = 0$ planes. Figure 16(a) shows that for installed cases, just downstream of the flap trailing edge ($x/D \approx 2.1$), the stress is nearly doubled relative to the isolated nozzle. The higher flap deflection broadens the increased turbulence level towards the centre of the plume as far as $8 - 10D$. The F08 case shows a small increase at $z/D \approx 0.25 - 0.5$ until $x/D = 5$ but becomes mixed into the main plume and is then similar to the isolated case. In the $z = 0$ plane below the wing (Fig. 16(b)), the F14 case shows an increase and broadening of the Reynolds stress profile and an increase at the centreline. Note the installed profiles are not symmetrical due to the finite span tapered wing.

Similar trends for the shear stresses are displayed in Fig. 17. The peak in the F14 shear stress in Fig. 17(a) is at a lower z/D position than the isolated of F08 cases due to greater flow deflection. Fig. 17(b) shows little effect for the

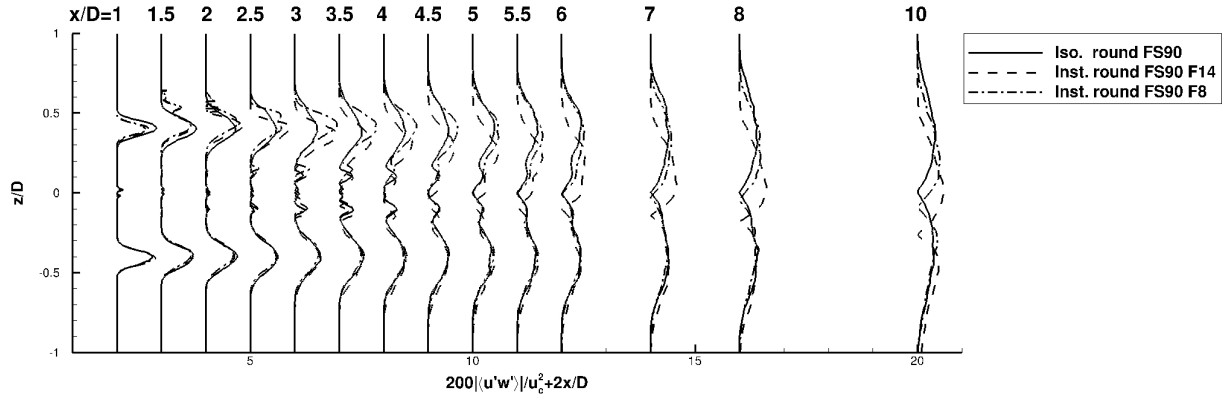

(a) $y = 0$ plane

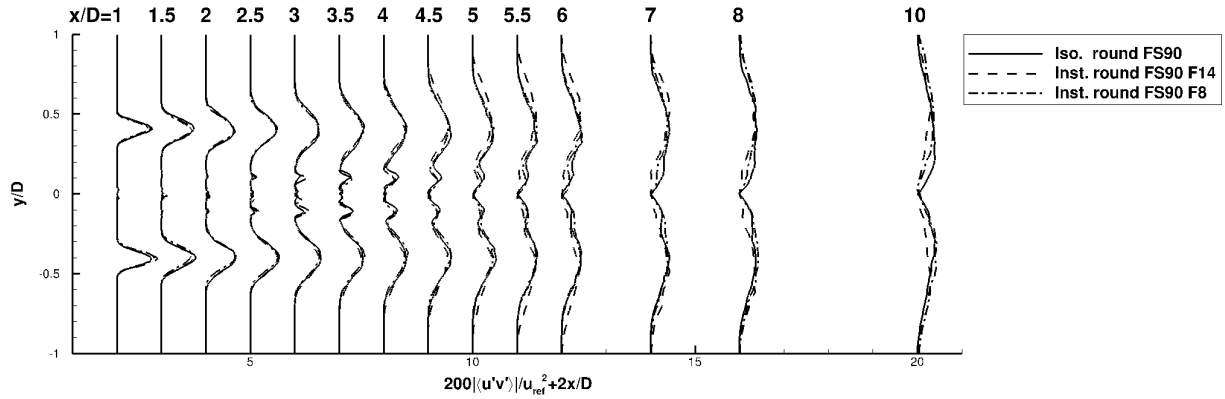

(b) $z = 0$ plane

Fig. 17 Reynolds shear stress profiles at $y = 0$ and $z = 0$ planes.

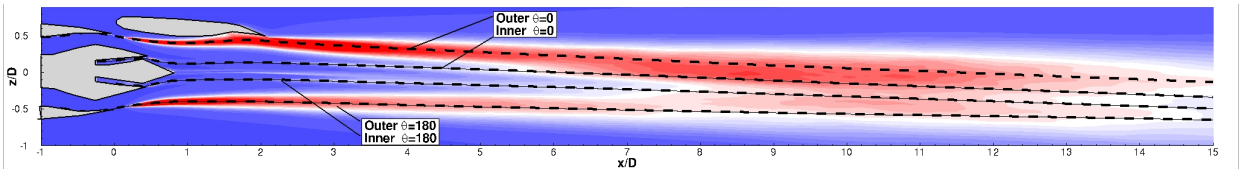

(a) y plane

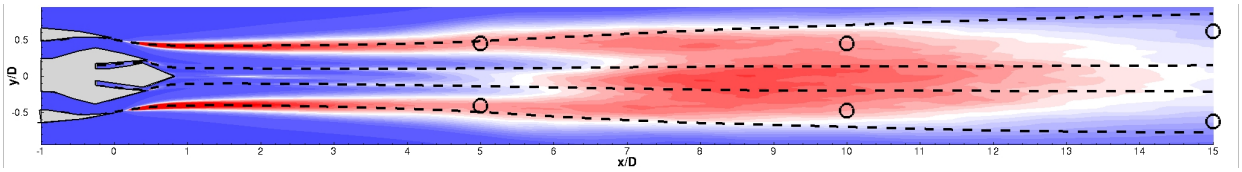

(b) z plane

Fig. 18 Example lip line profiles extracted from streamlines indicated by dashed lines.

F14 case except a small increase and profile broadening over the isolated case.

2. Lip line profiles

Figure 18 shows example lip lines to allow comparison of quantities along the length of the outer and inner shear layers. Due to the true 3-D nature of the installed cases, four azimuthal locations are chosen at 0 and 180 degrees (above and below the wing) and 90 and 270 degrees (inboard and outboard respectively). Streamlines are extracted similarly for each case and at each azimuthal location. Contours represent $\langle k \rangle$, symbols represent extracted points where k contours do not follow the streamlines. These are contrasted with the axi-symmetric isolated jet.

In the upper part of the outer shear layer displayed in figure 19(a), after the initial transition, two peaks can be seen. The first is due to jet shear layer interaction with the flap TE. The second larger peak is due to increased production from the flap downwash and the jet shear layer. For F14, Fig. 19(e) indicates the variation of $\langle k \rangle$ along the streamline with an increase in $\langle k \rangle$ below the flap just upstream of the TE, a small decay and further production from the accelerated flow downstream. This increase over the isolated case is maintained until $x/D \approx 18$. The effect is reduced for the F08 case compared to the F14 case, but both show increases in $\langle k \rangle$ of 10-70%. Surprisingly, at $\theta = 180$ (Fig. 19(b)) levels are similar for all cases. However, Figs. 19(c)-19(d) appear to indicate the increase in the upper shear layer is compensated downstream at each side. This is particularly prominent for the F14 case where there is a reduction after $x/D \approx 7$. However, k contours do not follow the streamlines in the z plane, hence sample points are extracted as indicated in Fig. 18(b) and are shown as symbols in Fig. 19(c)-19(d). These are in accord with the streamlines until $x/D = 5$. For the F14 case, $\langle k \rangle$ is greater or equal to the Iso. and F08 cases at $x/D = 10$, before falling below these at $x/D > 15$. This drop is partially caused by a more rapid axial decay combined with a redistribution of $\langle k \rangle$ in the y-axis. The ovalisation of the F14 plume can clearly be seen in Fig. 12, at $x/D > 5$, whilst the Iso. and F08 contours remain round. This demonstrates the need for more routine in-depth 3D analysis. The F08 case behaves similarly to the F14

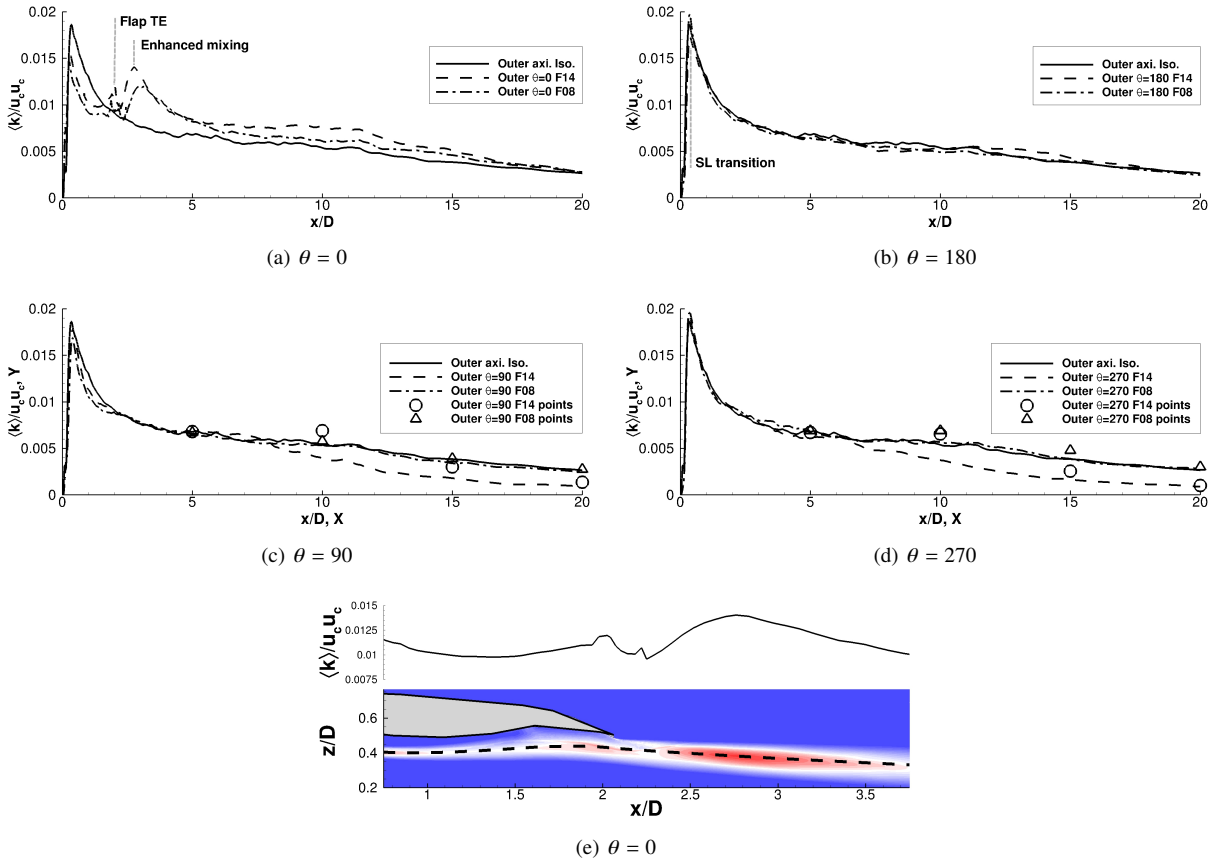

(a) $\theta = 0$

(b) $\theta = 180$

(c) $\theta = 90$

(d) $\theta = 270$

(e) $\theta = 0$

Fig. 19 (a-d) Turbulence kinetic energy in the outer shear layer at different azimuthal angles, (e) zoom of flap region (F14).

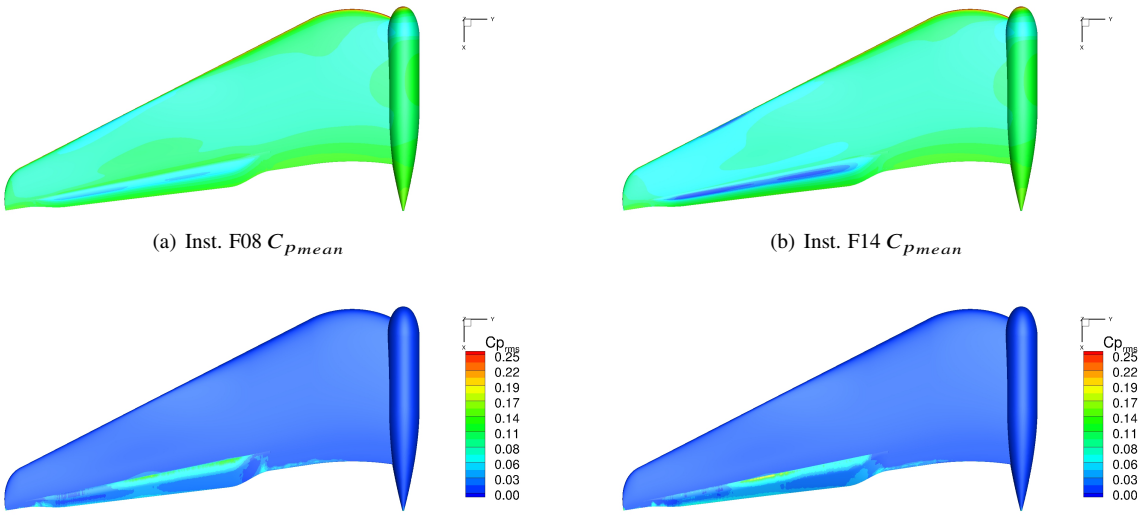

(a) Inst. F08 $C_{p_{mean}}$ (b) Inst. F14 $C_{p_{mean}}$

(c) Inst. F08 $C_{p_{rms}}$ (d) Inst. F14 $C_{p_{rms}}$

Fig. 20 $C_{p_{mean}}$ (a-b) and $C_{p_{rms}}$ (c-d) contours from above the two installed wings.

case at $x/D = 10$ but is otherwise similar to the Iso. case.

D. Wing and flap surface pressures

Figure 20 provides mean and *rms* pressure coefficient contours for both installed cases looking from above the wing. The $C_{p_{mean}} = (\langle p \rangle - p_a)/0.5\rho u_{FS}^2$ contours in frames (a)-(b) show the high flap angle has deepened the low pressure areas along the span of the flap recess, on the outboard side of the nozzle on the wing leading edge and on the suction side towards the wing tip. The $C_{p_{rms}} = (\langle p' \rangle - p_a)/0.5\rho u_{FS}^2$ contours in frames (c) and (d) show the F08 flap recess has a uniformly distributed area of fluctuating pressure along two thirds of the flap span (from the inboard side). An increase in the centre of the flap recess where the jet plume passes beneath is visible for the F14 case.

Figure 21 similarly plots pressure coefficients looking from below the wing. The F08 case (Fig. 21(a)) has a small spot in the centre of the flap where $C_{p_{mean}}$ is high only at the flap trailing edge. This is intensified for the F14 case (Fig. 21(b)) and an increase in pressure is also visible along the flap leading edge showing a stronger flow impingement. A similar story is evident in frames (c) and (d) for $C_{p_{rms}}$. For the F08 case, pressure fluctuations can be seen on the flap leading edge, and the underside of the wing and flap. Again, these appear intensified for the F14 case. This could in part be due to ingestion of the jet shear layer turbulence.

To visualise the wing-flap recess, $C_{p_{rms}}$ is contoured on the suction and pressure sides of the flap in Fig. 22. The F08 case (Fig. 22(a)) takes a more uniform value along the leading edge that is generally higher than that of the F14 case (Fig. 22(b)). This is due to the incidence of the separated flow from the wing recess and flow redistribution within the recess itself. Figures 22(c)-22(d) however show higher pressure fluctuations over a larger span on the flap pressure

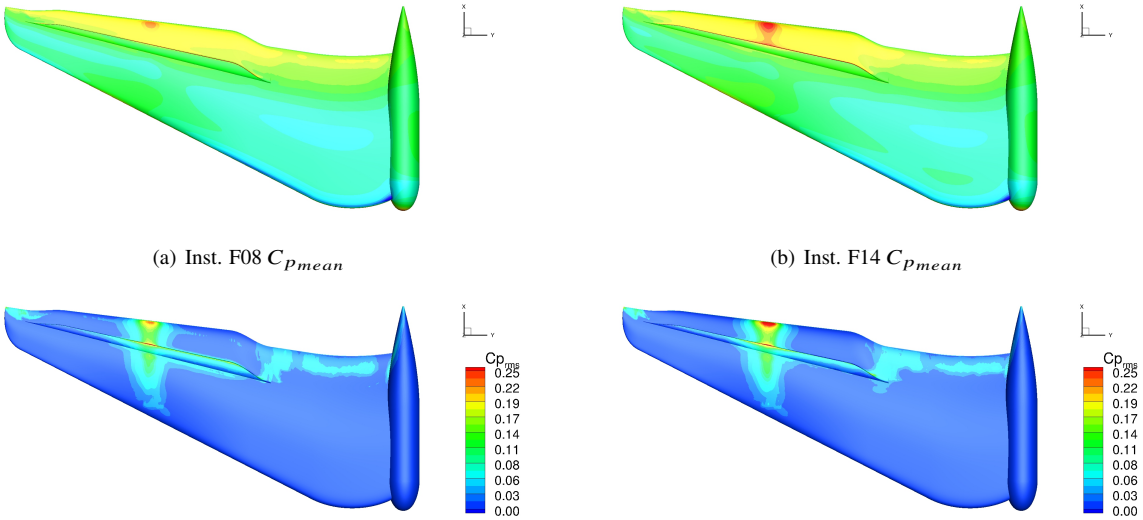

(a) Inst. F08 $C_{p_{mean}}$ (b) Inst. F14 $C_{p_{mean}}$

(c) Inst. F08 $C_{p_{rms}}$ (d) Inst. F14 $C_{p_{rms}}$

Fig. 21 $C_{p_{mean}}$ (a-b) and $C_{p_{rms}}$ (c-d) contours from below the two installed wings.

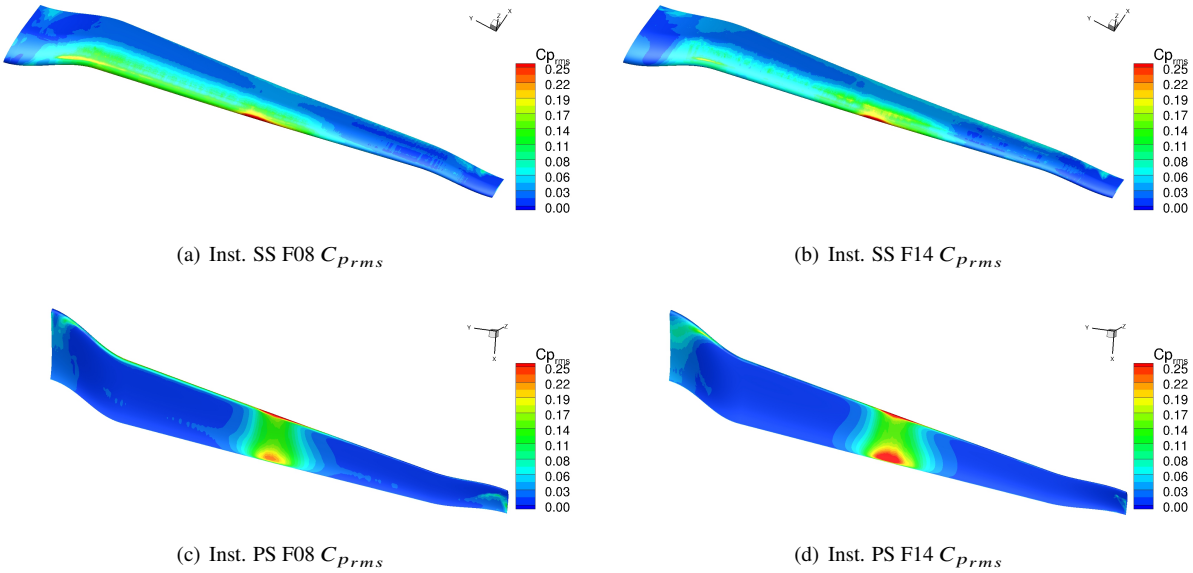

(a) Inst. SS F08 $C_{p_{rms}}$ (b) Inst. SS F14 $C_{p_{rms}}$

(c) Inst. PS F08 $C_{p_{rms}}$ (d) Inst. PS F14 $C_{p_{rms}}$

Fig. 22 Flap suction and pressure side $C_{p_{rms}}$ contours.

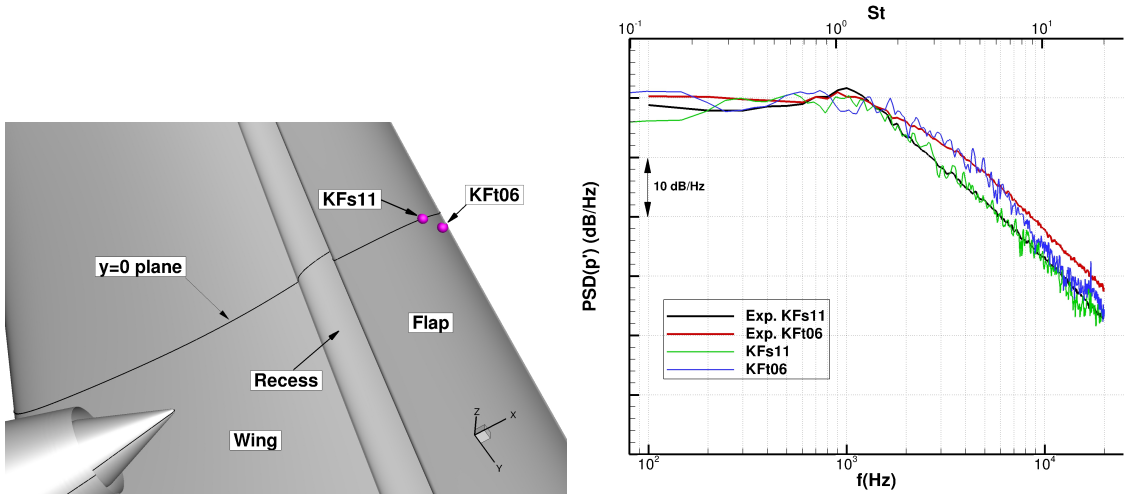

(a) (b)

Fig. 23 (a) Location of unsteady pressure probes (kulites for experiments), (b) power spectral density for unsteady pressure probes.

side for the F14 case in line with the jet axis. This side is directly exposed to the jet shear layer.

1. Pressure spectra

Figure 23(a) indicates the location of unsteady pressure probes on the surface of the wing and flap. Surface pressure spectra for these are shown in Fig. 23(b) and compared with measurements. Figure 23(b) shows spectra for the flap pressure side. The grid filter is expected to be at around 15 kHz. Probes KFs11 and KFt06 lie near the flap trailing edge and indicate excellent agreement with the measured spectra. This is an important aspect as the flap trailing edge is responsible for a large portion of the installed noise sources. The flap chord and local convective speed correspond to 1200 Hz. Higher frequencies are generated by the jet shear layer. Lower frequencies relate to large scale effects such as unsteady lift.

E. Space-time correlations

Velocity second and fourth order space-time correlations are extracted from unsteady data to reveal changes in length and time scales and dominant sources. These complete (and the 3D unsteady dataset recorded will surpass) the list of data obtainable by advanced PIV as presented by Bridges and Wernet [48]. The formulae are as follows

$$R_{ij}(x,\Delta,\tau) = \frac{\langle u_i'(x,t)u_j'(x+\Delta,t+\tau)\rangle}{\langle u_i'(x,t)u_j'(x,t)\rangle} \tag{6}$$

$$R_{ijkl}(x,\Delta,\tau) = \langle(\rho u_i'u_j' - \langle\rho u_i'u_j'\rangle)(x,t)\cdot(\rho u_k'u_l' - \langle\rho u_k'u_l'\rangle)(x+\Delta,t+\tau)\rangle \tag{7}$$

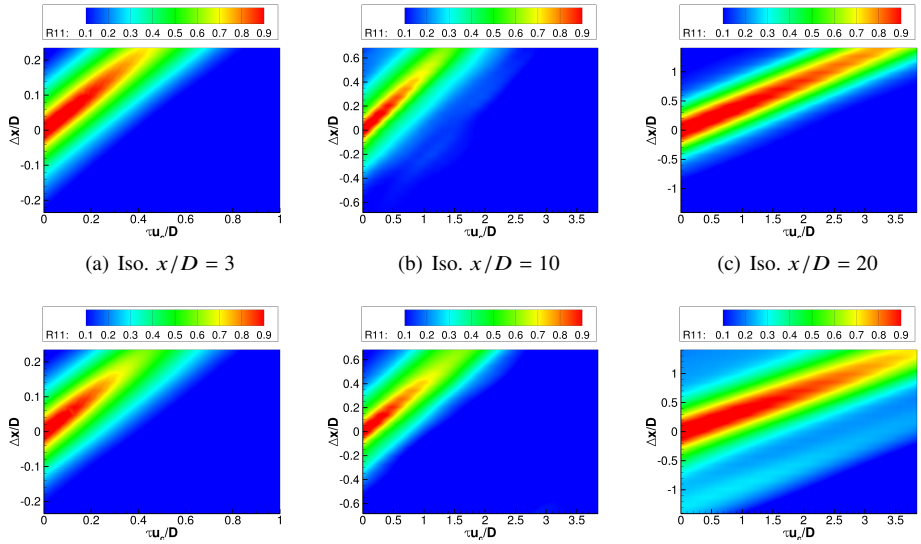

(a) Iso. $x/D = 3$ (b) Iso. $x/D = 10$ (c) Iso. $x/D = 20$

(d) F14 $x/D = 3$ (e) F14 $x/D = 10$ (f) F14 $x/D = 20$

Fig. 24 Second order space-time correlation contours (R_{11}) along the outer shear layer ($z > 0$).

Second order space-time correlations (R_{ij}) in the outer shear layer (at $\theta = 0$) are provided in Fig. 24 at different axial locations. The $y - z$ location is changed with each case using a short time mean to follow the maximum flow gradient in the outer shear layer and are indicated in Fig. 8. Equivalent positioning of probes between cases was difficult downstream as flow gradients become weaker and more poorly averaged on short time scales than those found nearer the geometry.

The gradient of the contours shown in Fig. 24 indicate the convective speed of vortices in the flow. This varies from approximately $0.55u_c$ at $x/D = 3$, $0.49u_c$ at $x/D = 10$ to $0.44u_c$ at $x/D = 20$. The F14 contours indicate a more rapid decay rate, convective speed falling to $0.41u_c$ and $0.36u_c$ at $x/D = 10$ and 20 respectively.

Figure 25(a) shows 4^{th}-order space time correlation amplitudes (R_{ijkl}/u_c^4) for the three cases studied at $x/D = 3$ (downstream of the flap for installed cases). These represent the magnitude of Goldstein analogy [49] sources. Similar 4^{th} order correlations have been used by Karabasov et al. [50] to improve jet acoustics models. Here, we provide the maximum amplitude of each component to give an indication of relative source strengths and distribution. More in depth analysis of the sound sources is required for a detailed picture but is outside the scope of this paper, as is prediction of far-field sound using such an analogy, as this is already provided by the FWH method. For each significant component, an increase in magnitude is evident when the wing-flap is included. This is most obvious for the F14 case. The installed cases show a factor of 2.5 and 3.5 increase in R1111 compared to the isolated jet for the F08 and F14 cases respectively. For a more detailed picture other locations will need to be assessed.

At $x/D = 10$ no trend is immediately obvious. Broadly speaking the magnitudes between cases could be considered similar. This region is near the merging of the shear layers (see Fig. 15), however levels are greatly reduced over those

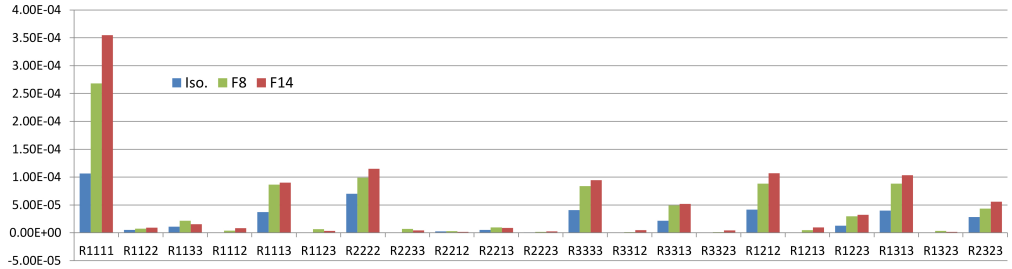

(a) $x/D = 3$

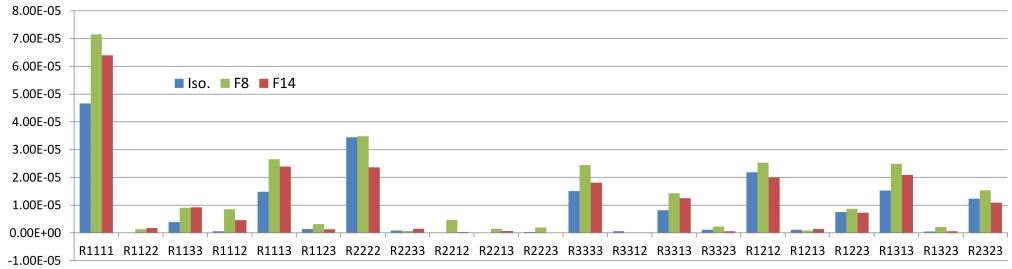

(b) $x/D = 10$

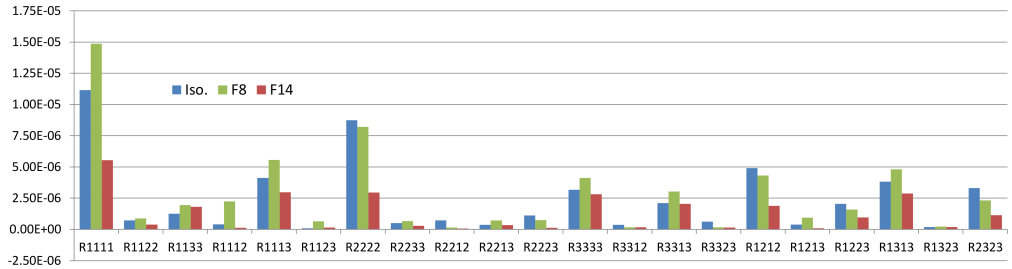

(c) $x/D = 20$

Fig. 25 4^{th}**-order space-time correlation components** $(R_{ijkl}(x,\Delta,\tau)/u_c^4)$ **at** $x/D = 3,10$ **and** 20 **in the outer shear layers of each case at** $\theta = 0$**.**

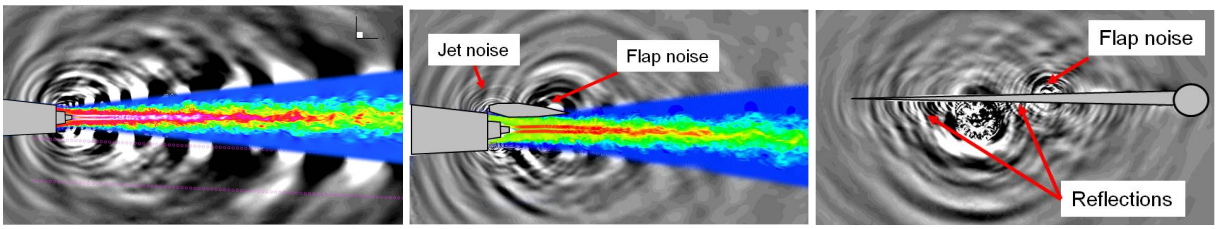

(a) Iso. FS90 $y = 0$ plane (b) Inst. FS90 F14 $y = 0$ plane (c) Inst. FS90 F14 $x \approx 1D$ plane

Fig. 26 Instantaneous dp/dt contours for the isolated and F14 case at different plane locations with axial velocity contours in the jet plume region.

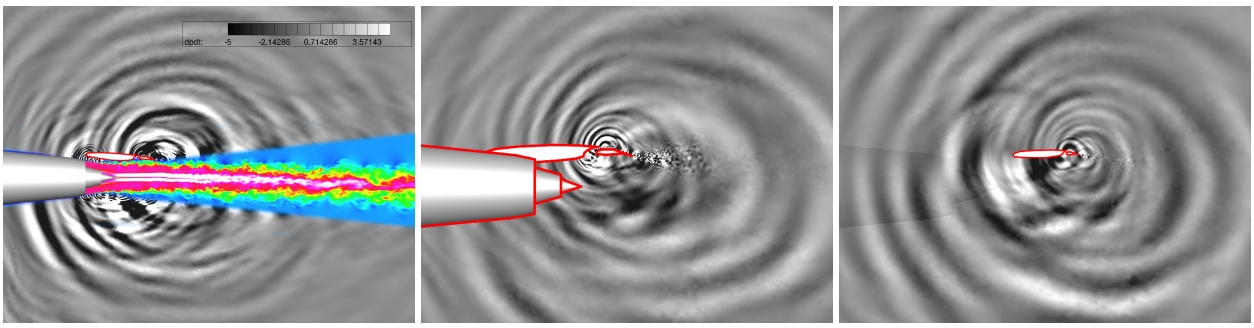

(a) F14 $y = 0$ plane (b) F14 $y = 2D$ plane (inboard) (c) F14 $y = -2D$ plane (outboard)

Fig. 27 Instantaneous dp/dt contours for the F14 case at different $y-$planes with axial velocity contours in the jet plume region.

at $x/D = 3$ by a factor of 2-5. The components of the installed cases are still greater than the isolated jet by a factor of approximately 1.5. The F08 case increases turbulence in the upper, outer shear layer but does not cause a substantial change in jet decay rate, hence the 8^o flap angle displays higher 4^{th}-order components than the F14 case overall. This may also be in part due to the location of the F08 and F14 probes. Although, equivalent probe positioning is difficult to achieve, we expect to capture the trend. The F14 case generally shows higher components than the isolated nozzle, for example R1111-R1112, R1113, R3333, R3313, R1313.

Figure 25(c) shows components further downstream at $x/D = 20$. Again a significant drop in levels by a factor of around 3 is observed. The main difference is a reduction in the F14 components relative to the isolated and F08 cases. This could be due to a more rapid decay of the F14 turbulence due more intense mixing downstream of the flap and on shear layer merging.

F. Acoustics

1. Instantaneous dp/dt contours

Figure 26 displays dp/dt contours for the isolated and installed nozzle (F14). The isolated nozzle (Fig. 26(a)) shows a spherical source with waves convected downstream. For the installed case in Fig. 26(b), the flap clearly generates a

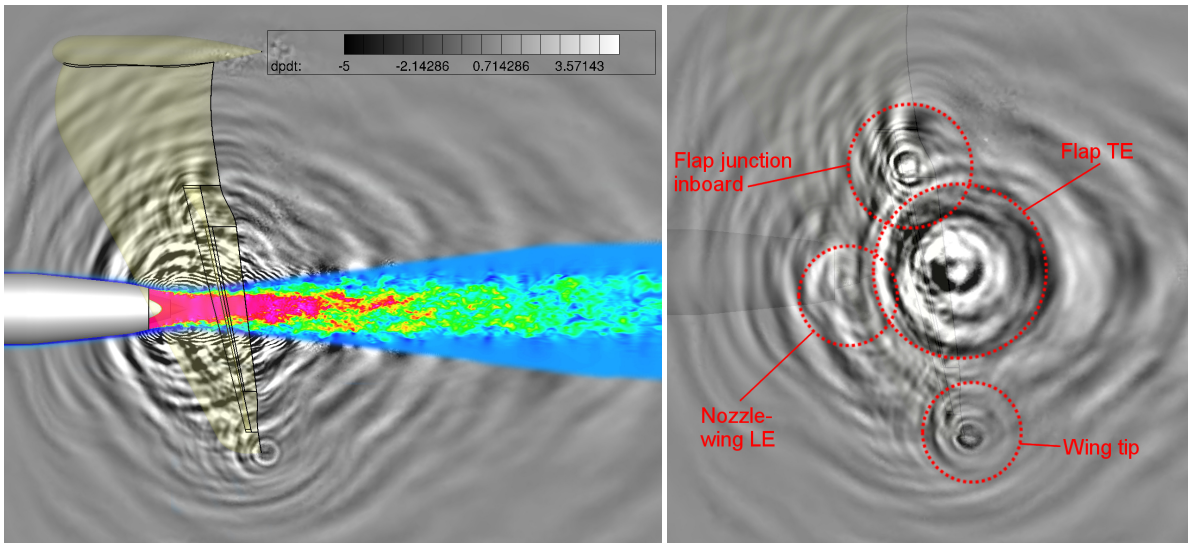

(a) F14 $z = 0.25D$ plane (b) F14 $z = 1D$ plane

Fig. 28 Instantaneous dp/dt contours for the F14 case at different $z-$planes with axial velocity contours in the jet plume region.

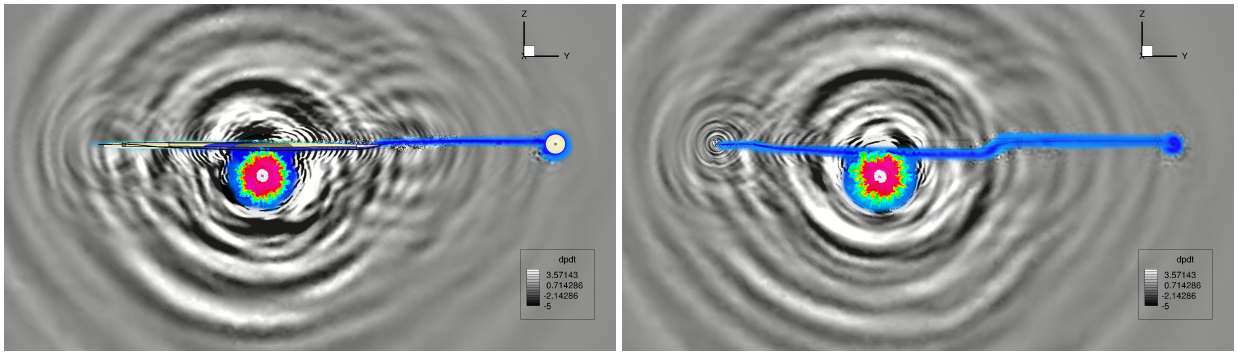

(a) F14 $x = 1.67D$ plane (b) F14 $x = 2.5D$ plane

Fig. 29 Instantaneous dp/dt contours for the F08 and F14 cases at different $x-$planes with axial velocity contours in the jet plume region.

large local noise source. This region is also known to refract acoustic waves over the wing. The location of the installed nozzle allows high frequency waves to reflect off the wing leading edge. Figure 26(c) clearly shows reflection of waves off the underside of the wing and small and large scale acoustic waves emanating from the flap region. Of interest is the effect of turbulence ingested from the jet shear layer into the flap recess, where the flow is then accelerated before exiting along the flap upper surface. This is akin to slat noise as presented by Deck and Laraufie [51].

Figure 27(a) gives an overview of the pressure waves in the $y = 0$ plane. The accelerated fluid in the wing-flap recess generates a source when it meets the trailing edge on the upper wing surface of the flap cove. Waves also reflect within the cavity and back towards the ground. Both ends of the flap appear to be significant sources. Figure 27(b) shows dp/dt contours at a plane near the inboard flap extent and Fig. 27(c) shows a plane at the outboard flap extent. In both figures, waves can be seen emanating from above the flap and the flap TE. The higher flap deflection produces more intense waves but the contours are overall similar for the F08 case.

To provide a more global picture of the acoustic field, dp/dt contours in the $z = 0.25D$ plane below the wing are shown in Fig. 28(a). Below the wing noise sources can be seen at the flap extremities where the jet and the flight stream impinge on the flap. These are more clearly seen in Fig. 28(b) which are above the wing at $z = 1D$. In the centre lies the main installation noise source from the flap with smaller sources at the wing-flap junctions and wing tip. Some jet and installation noise is reflected between the wing leading edge and nacelle. Looking down on the wing as shown, part of the nozzle exit is exposed and this allows more noise to travel upwards. This is visible on the left side of the main flap source (approximately an 8-O'clock position) and is more well defined for the F14 case.

Figure 29(a) shows an axial plane near the middle of the flap. Above the wing on the right, high frequency noise downstream of the wing-flap recess can be seen and is mostly absent on the upper left which is upstream of the gap due to sweep. The gap is wider below the wing and high frequency waves can be seen along most of the bottom of the flap. High frequency waves above the wing recess may be generated by accelerated turbulent flow passing the recess trailing edge of the wing. High frequency noise may also be generated below the recess by flow separated from the wing recess, impinging on the flap LE. Downstream of the flap TE at $x/D = 2.5$, Fig. 29(b) also clearly shows waves from the flap, flap extremities and wing tip. Similarly on the right (inboard) side of Fig. 29(b), inboard flap and wing tip sources can be observed.

2. Overall sound pressure level

Figure 30 compares OASPL polar arc profiles for each installed case with the azimuthally averaged isolated jet. Figure 30(a) represents azimuthal angles $0 < \theta < 130$ and 30(b) azimuthal angles $180 < \theta < 310$. The isolated, F08 and F14 cases use symbols, dashed and solid lines respectively. Clearly there is a large installation effect particularly at higher polar angles. Overall the trends and shapes are similar between the two flap angles. A small increase in noise above the wing is observed at $\theta = 0, 50$ and 310^o for the F08 case at polar angles greater than 80^o. For azimuthal angles

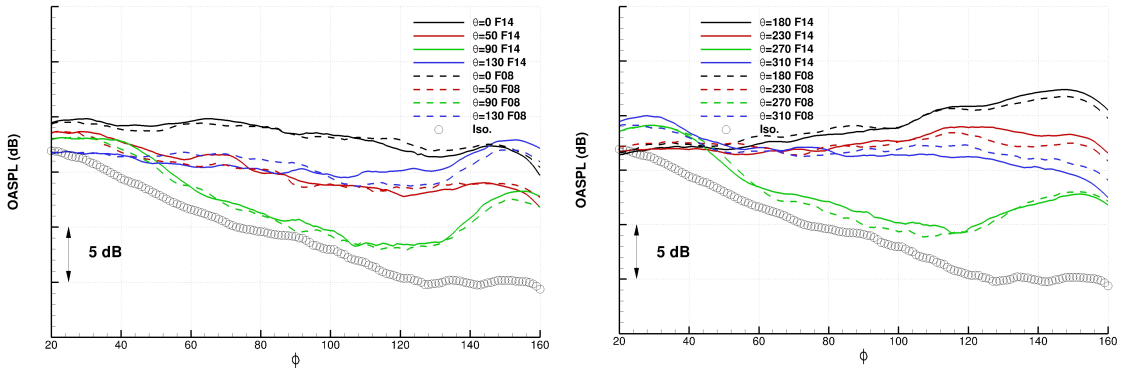

(a) $0 < \theta < 130^o$ (b) $180 < \theta < 310^o$

Fig. 30 Far-field OASPL polar arcs at different azimuthal angles.

below the wing ($90 \leq \theta \leq 270$), noise is lowered by lowering the flap angle, the effect being greatest on the outboard side ($\theta = 270^o$).

The flap trailing edge and its vicinity is a significant noise source absent from the isolated case. At the wing inboard ($\theta = 90^o$) and outboard ($\theta = 270^o$) directions, sound waves are blocked by the wing-flap geometry and noise is instead reflected downwards. Most noise is hence directed beneath the wing. The higher flap deflection causes more noise to be generated in the inboard and outboard sideline directions ($\theta = 130^o$ and $\theta = 230^o$) respectively for $\phi > 100^o$. Above the wing, installation effects create more upstream noise relative to the isolated jet, but this region does not receive reflected noise from the jet plume. Most installation noise appears in the upstream direction ($\phi > 90^o$).

The shielding effect above the wing is limited due to the short chord of the wing over the jet centreline and small section of wing span interacting with the jet plume. Effects of finite span and surface length downstream of the nozzle exit on shielding have been investigated by Brown [10, 52]. The current geometry lies in the region studied where shielding effects are expected to be low. The F08 case however generates more noise above the wing than the F14 case. The flyover profile passes near the maximum OASPL for both installed cases. Overall, the main difference between the two flap deflections appears to be a small change in directivity.

3. Sound pressure level spectra

Figure 31 shows SPL spectra at flyover (FO) and outboard sideline (SL) azimuthal angles at polar locations of $\phi = 30, 60, 90, 120, 150^o$. With increasing polar angle ϕ, the installation effect becomes more pronounced. At a polar angle of 30^o the isolated F14 and F08 cases appear similar. Most of the noise in this direction is hence attributed to mid-low frequency noise generated upstream due to installation effects and low frequency flow at the downstream end of the jet plume. There is a small increase in noise at both FO and SL locations (Fig. 31(a)-31(b)), in the same frequency range as the installation noise at higher polar angles. At $\phi = 60^o$ (Fig.31(c)-31(d)), a peak above the isolated SPL is noted at $f = 700$ Hz. The SL spectra in Fig.31(d) has a more broadband shape in the range $400 < f < 4000$

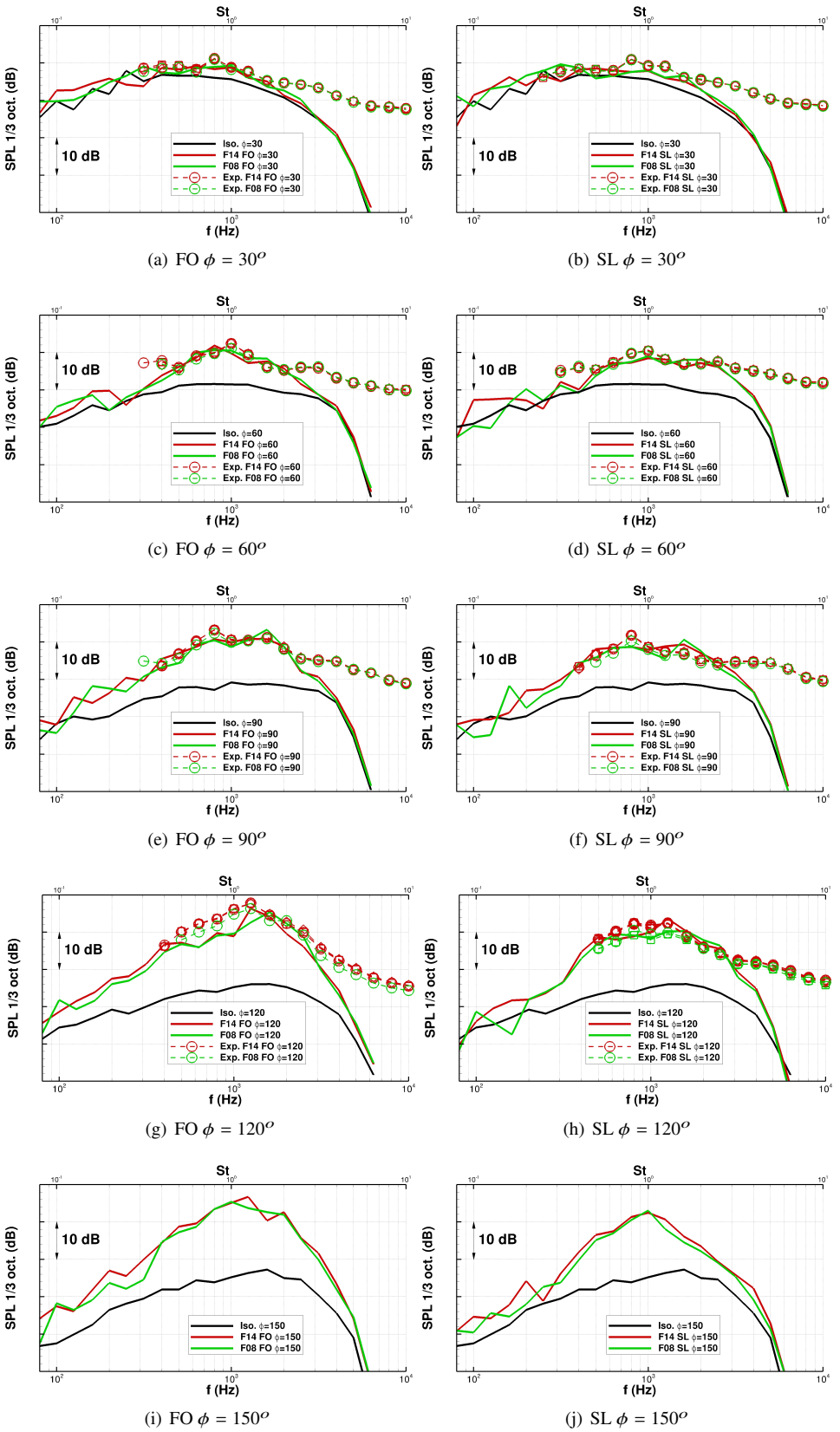

(a) FO $\phi = 30^o$ (b) SL $\phi = 30^o$

(c) FO $\phi = 60^o$ (d) SL $\phi = 60^o$

(e) FO $\phi = 90^o$ (f) SL $\phi = 90^o$

(g) FO $\phi = 120^o$ (h) SL $\phi = 120^o$

(i) FO $\phi = 150^o$ (j) SL $\phi = 150^o$

Fig. 31 SPL spectra at flyover (FO) and outboard sideline (SL) azimuthal angles at polar locations of $\phi = 30, 60, 90, 120, 150^o$.

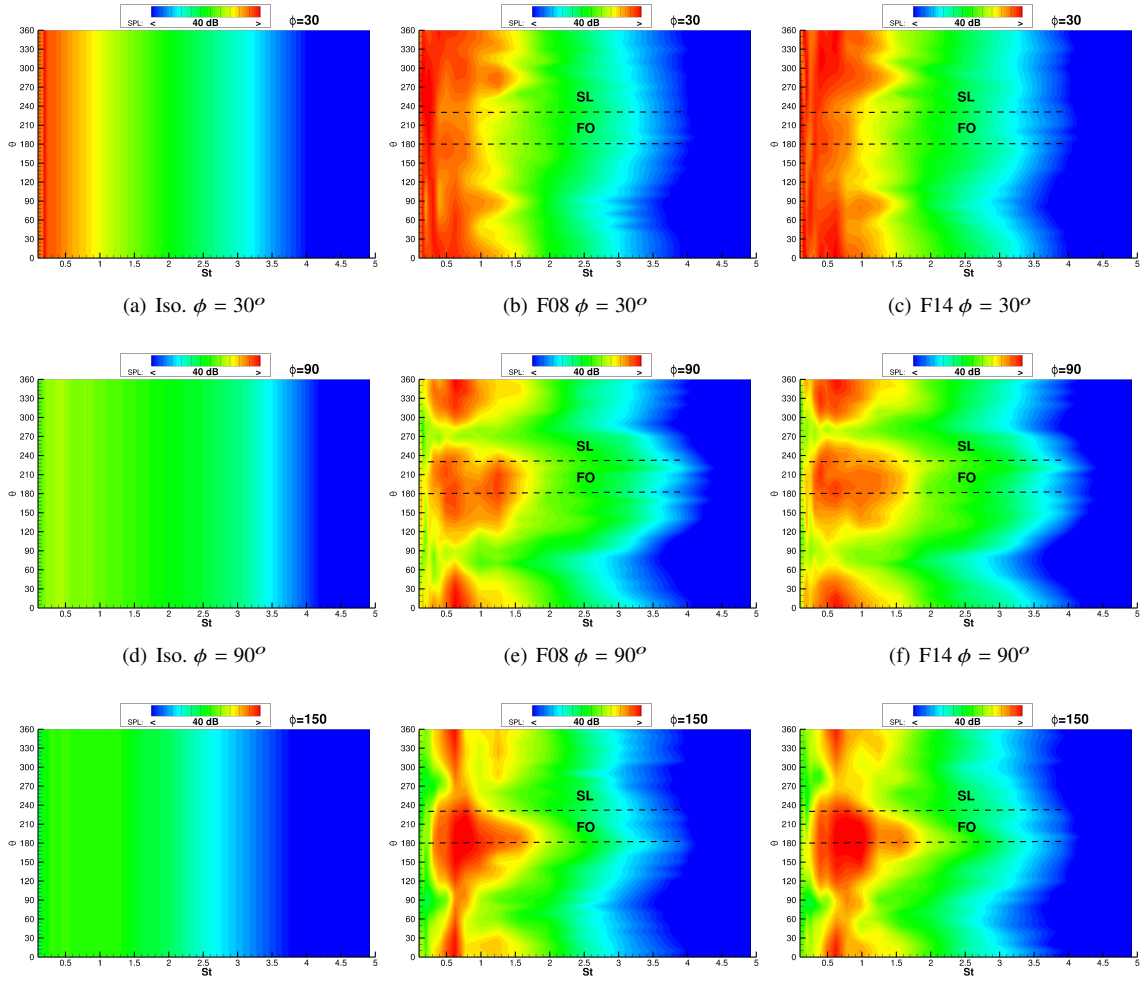

(a) Iso. $\phi = 30^o$ (b) F08 $\phi = 30^o$ (c) F14 $\phi = 30^o$

(d) Iso. $\phi = 90^o$ (e) F08 $\phi = 90^o$ (f) F14 $\phi = 90^o$

(g) Iso. $\phi = 150^o$ (h) F08 $\phi = 150^o$ (i) F14 $\phi = 150^o$

Fig. 32 SPL contours plotted against azimuthal position and St for polar locations $\phi = 30, 60, 90, 120, 150^o$.

Hz compared to FO due to jet mixing and interference of different frequency waves from the jet, flap and wing tip. At $\phi = 90^o$ (Fig. 31(e)-31(f)), the FO and SL spectra are similar except for a small increase of noise below $f = 300$ Hz for FO. These, including the measurements, both exhibit a double peak, noted by Mengle [13] when the gulley height between the wing and nozzle is small, or the flap TE is close to the jet. As suggested by Mengle, this could be a selective amplification of frequencies within both the inner and outer shear layers. In Figs 31(g) to 31(j), the trend is similar with increasing SPL levels and a sharpening of the peak near $f = 1000$ Hz. Measurements are not available for $\phi = 150^o$. The LES-RANS show peak increases of 20 dB. At similar conditions, Mengle [13] obtains an increase compared to an isolated nozzle of approximately 10 dB under static conditions, and 15 db with a flight stream of $M = 0.28$. This indicates good consistency for similar conditions and supports validity of the LES-RANS solutions.

The spectral content at other azimuthal locations is contoured in Fig. 32. The isolated case is azimuthally averaged. The variation of SPL contours with azimuthal location and Strouhal number ($St = fD/u_c$) for installed cases at different

polar angles are presented. At $\phi = 30^o$ (Fig. 32(b)-32(c)), there is relatively low influence from the upstream wing-flap geometry except for two weak peaks and most noise is in the low frequencies ($St < 1$). The peak SPL is similar to the isolated case. The peaks become more defined at higher polar angles where installation noise dominates. At $\phi = 90^o$ (Fig. 32(e)-32(f)) the azimuthal variation becomes more defined and both high and particularly low frequencies are more prominent below ($\theta = 180$) and above ($\theta = 0$) the wing. This shows a strong upstream influence due to installation effects. At $\phi = 150^o$, a strong sharper peak is observed at $\theta = 180$ and a narrow band of low frequency noise is evident at all azimuthal locations.

The overall similarity of the F08 and F14 acoustics suggests the trailing edge proximity to the jet is the main installation source due to scattering of waves. Mockett et al. [53] show up to 7.5 dB noise reduction when the wing is moved vertically away from the jet. The vertical movement of the flap is much smaller between the F14 and F08 cases. The F08 case modifies the upper jet plume but this effect is relatively small compared to the large source introduced by the presence of a surface near the nozzle. The suppression of turbulence in the vicinity of the flap, leads to a rapid growth in turbulence kinetic energy downstream. A similar rapid growth in turbulence length and time scales coincide with a peak in R1111 as shown by Tyacke [54] suggesting instability waves could be responsible for the trailing edge noise source.

VI. Conclusion

A hybrid LES-RANS methodology for the prediction of installed jet noise has been developed. The method presented is quite general and could be used to reliably predict noise for a wide range of jets or landing gear. Using this, flow and noise produced by a round, ultra-high bypass-ratio aeroengine nozzle with a hot core and outer flight stream has been studied. Additionally, installation effects for a wing-flap geometry with flap angles of 8 and 14 degrees have been investigated. Results have been shown to match with available measurements for acoustics and surface pressure spectra. This is essentially a blind test, as data was available after the simulations were completed. The close coupling of the wing-flap geometry and UHBPR jet nozzle produces strong noise sources. An increase of 20 dB was predicted at high polar angles reducing towards the jet axis downstream.

The LES-RANS has provided detailed data for modern engine nozzles and jet-airframe interaction which is difficult to acquire experimentally. Installation effects introduce strong polar and azimuthal variations in OASPL. Upstream polar angle noise is increased above and below the wing with a degree of shielding above the wing. The increase in SPL is particularly prominent in the range of $0.1 < St < 1.5$ at upstream polar angles.

A small effect of flap angle on acoustics directivity was found relative to the large source introduced by the presence of the wing and flap trailing edge. The reduced flap deflection of the F08 case had a smaller but still pronounced effect on $\langle k \rangle$ and $\langle p' \rangle$, although only a minimal effect on the overall noise levels relative to the F14 case. The reduced impingement on the flap trailing edge reduced jet plume deflection, $\langle k \rangle$ azimuthal redistribution and $\langle k \rangle$ and $\langle p' \rangle$

magnitudes. This changed acoustic directionality and the amount of mixing noise. The F08 flow similarities with the isolated jet indicate most of the installation noise is produced by the direct and downstream interaction of the flap trailing edge with the jet shear layer.

Second order space-time correlations have provided spatial and temporal scales indicating a higher turbulence decay rate for installed cases. Using fourth order space-time correlations, changes in source strength and location have been identified. Near the wing, the dominant noise source is approximately 2.5-3.5 times higher than the isolated jet. By $x/D = 10$, this is reduced to a factor of approximately 1.5. The full space-time correlations can be used to improve acoustics models. It is expected that further analysis will help unlock the underlying noise generation mechanisms to aid design of future low noise aircraft.

Acknowledgements

The authors would like to acknowledge the collaboration with C. Mockett of CFD Software E-F GmbH, Berlin, for the hybrid meshing strategies presented. Computing time is greatly appreciated from both the United Kingdom Turbulence Consortium (UKTC), EPSRC EP/L000261/1 and the UK national computing facility ARCHER. The work was performed in the EU-funded project "JERONIMO" (ACP2-GA-2012-314692-JERONIMO).

References

[1] Commission, E., "Flightpath 2050 Europe ' s Vision for Aviation," Tech. rep., 2011. doi:10.2777/50266.

[2] Viswanathan, K., Czech, M. J., and Lee, I. C., "Towards Prediction of Dual-Stream Jet Noise: Database Generation," *49th AIAA Aerospace Sciences Meeting including the New Horizons Forum and Aerospace Exposition*, AIAA, Orlando, Florida, 2011.

[3] Thomas, R. H., "Aeroacoustics of Propulsion Airframe Integration : Overview of NASA ' s Research," *NOISE-CON*, Cleveland, Ohio, 2003, pp. 8, paper 105.

[4] Viswanathan, K., Underbrink, J. R., and Brusniak, L., "Space-Time Correlation Measurements in Nearfields of Jets," *AIAA Journal*, Vol. 49, No. 8, 2011, pp. 1577–1599. doi:10.2514/1.J050750, URL `http://arc.aiaa.org/doi/abs/10.2514/1.J050750`.

[5] Bridges, J. E., and Wernet, M. P., "Effect of Temperature on Jet Velocity Spectra," *13th AIAA/CEAS/28th AIAA Aeroacoustics Conference*, AIAA, AIAA and CEAS, 2007, pp. Paper number 2007–3628. doi:10.2514/6.2007-3628.

[6] Fleury, V., Bailly, C., Jondeau, E., Michard, M., and Juvé, D., "Space – Time Correlations in Two Subsonic Jets Using Dual Particle Image Velocimetry Measurements," *AIAA Journal*, Vol. 46, No. 10, 2008, pp. 2498–2509. doi:10.2514/1.35561.

[7] Mengle, V., Elkoby, R., Brusniak, L., and Thomas, R. H., "Reducing Propulsion Airframe Aeroacoustic Interactions with Uniquely Tailored Chevrons: 1. Isolated Nozzles," *12th AIAA/CEAS Aeroacoustics Conference (27th AIAA Aeroacoustics*

Conference), , No. May, 2006, p. 2467. doi:10.2514/6.2006-2435, URL http://arc.aiaa.org/doi/abs/10.2514/6.2006-2435.

[8] Mengle, V., Elkoby, R., Brusniak, L., and Thomas, R. H., "Reducing Propulsion Airframe Aeroacoustic Interactions with Uniquely Tailored Chevrons: 2. Installed Nozzles," *12th AIAA/CEAS Aeroacoustics Conference (27th AIAA Aeroacoustics Conference)*, , No. May, 2006, pp. 1–15. doi:10.2514/6.2006-2435, URL http://arc.aiaa.org/doi/abs/10.2514/6.2006-2435.

[9] Mengle, V., Brusniak, L., Elkoby, R., and Thomas, R. H., "Reducing Propulsion Airframe Aeroacoustic Interactions with Uniquely Tailored Chevrons: 3. Jet-Flap Interaction," *12th AIAA/CEAS Aeroacoustics Conference (27th AIAA Aeroacoustics Conference)*, , No. May, 2006, p. 2435. doi:10.2514/6.2006-2435, URL http://arc.aiaa.org/doi/abs/10.2514/6.2006-2435.

[10] Brown, C., "Including Finite Surface Span Effects in Empirical Jet-Surface Interaction Noise Models," *AIAA Scitech*, AIAA, 2016, p. 14 pages. doi:10.2514/6.2016-0006.

[11] Brown, C., Podboy, G., and Glenn, N., "Jet-Surface Interaction Noise from High-Aspect Ratio Nozzles : Test Summary," *AIAA Aviation*, AIAA, 2017, p. 30 pages. doi:10.2514/6.2017-3522.

[12] Thomas, R. H., Czech, M. J., and Doty, M. J., "High Bypass Ratio Jet Noise Reduction and Installation Effects Including Shielding Effectiveness," *51st AIAA Aerospace Sciences Meeting including the New Horizons Forum and Aerospace Exposition*, , No. January, 2013, pp. AIAA 2013–0541. doi:10.2514/6.2013-541.

[13] Mengle, V., "The Effect of Nozzle-to-Wing Gulley Height on Jet Flow Attachment to the Wing and Jet-Flap Interaction Noise," *Aiaa 2011-2705*, , No. June, 2011, pp. 5–8. doi:10.2514/6.2011-2705.

[14] Pope, S. B., *Turbulent Flows*, Cambridge University Press, 2000.

[15] Nallasamy, M., "Survey of Turbulence Models Jet for the Computation of Turbulent Flow and Noise," Tech. rep., NASA, 1999.

[16] Georgiadis, N., Yoder, D., and Engblom, W., "Evaluation of modified two-equation turbulence models for jet flow predictions," *AIAA journal*, , No. January, 2006, pp. 1–16. doi:10.2514/1.22650, URL http://arc.aiaa.org/doi/pdf/10.2514/1.22650.

[17] Georgiadis, N. J., and DeBonis, J. R., "Navier-Stokes analysis methods for turbulent jet flows with application to aircraft exhaust nozzles," *Progress in Aerospace Sciences*, Vol. 42, No. 1, 2006, pp. 377–418. doi:10.1016/j.paerosci.2006.12.001.

[18] Tam, C. K. W., Viswanathan, K., Ahuja, K. K., and Panda, J., "The sources of jet noise: experimental evidence," *Journal of Fluid Mechanics*, Vol. 615, 2008, p. 253. doi:10.1017/S0022112008003704.

[19] Freund, J. B., "Noise Sources in a Low-Reynolds-Number Turbulent Jet at Mach 0.9," *Journal of Fluid Mechanics*, Vol. 438, No. 0, 2001, pp. 277–305. doi:10.1017/S0022112001004414.

[20] Bres, G. A., Nichols, J. W., Lele, S. K., and Ham, F. E., "Towards Best Practices for Jet Noise Predictions with Unstructured Large Eddy Simulations," *42nd AIAA Fluid Dynamics Conference and Exhibit*, AIAA, New Orleans, Louisiana, 2012, pp. 1–21. URL http://scholar.google.com/scholar?hl=en{&}btnG=Search{&}q=intitle:Towards+Best+Practices+for+Jet+Noise+Predictions+with+Unstructured+Large+Eddy+Simulations{#}0.

[21] Debonis, J. R., "Prediction of Turbulent Temperature Fluctuations in Hot Jets," *23rd AIAA Computational Fluid Dynamics Conference*, AIAA, 2017, pp. 1–25. doi:10.2514/6.2017-3610.

[22] Xia, H., Tucker, P. G., Eastwood, S., and Mahak, M., "The influence of geometry on jet plume development," *Progress in Aerospace Sciences*, Vol. 52, No. 0, 2012, pp. 56–66. doi:10.1016/j.paerosci.2011.12.003, URL http://www.sciencedirect.com/science/article/pii/S0376042112000127.

[23] Vogel, P., Bin, J., and Sinha, N., "LES predictions of jet noise for a pylon-mounted dual stream nozzle and jet surface interactions," *ASME Turbo Expo 2016*, ASME, Seoul, South Korea, 2016, pp. V02AT41A012–V02AT41A012.

[24] Lee, H., Uzun, A., and Hussaini, M. Y., "Identification of jet noise source using causality method based on large-eddy simulation of a round jet flow," *International Journal of Aeroacoustics*, Vol. 16, No. 1-2, 2017, pp. 78–96. doi:10.1177/1475472X16680465.

[25] Mendez, S., Shoeybi, M., Lele, S. K., and Moin, P., "On the use of the Ffowcs Williams-Hawkings equation to predict far-field jet noise from large-eddy simulations," *International Journal of Aeroacoustics*, Vol. 12, No. 1+2, 2013, pp. 1–20. doi:10.1260/1475-472X.12.1-2.1.

[26] Wang, Z.-N., Naqavi, I. Z., Mahak, M., Tucker, P., Yuan, X., and Strange, P., "Far Field Noise Prediction of Subsonic Hot and Cold Jets Using Large-Eddy Simulation," *Proceedings of ASME Turbo Expo 2014*, ASME, Dusseldorf, Germany, 2014, pp. 1–11. doi:10.1115/GT2014-27290.

[27] Nelson, C., Cain, A., Du, Y., Morris, P., and Spyropoulos, J., "Toward Efficient Computational Aeroacoustic Analysis of High Speed Jets," *ASME Turbo Expo 2013*, ASME, San Antonio, Texas, 2013, pp. 1–14. doi:10.1115/GT2013-94703.

[28] Tyacke, J. C., Naqavi, I. Z., Wang, Z.-N., Tucker, P. G., and Boehning, P., "Predictive Large Eddy Simulation for Jet Aeroacoustics - Current Approach and Industrial Application," *Journal of Turbomachinery*, Vol. 139, No. 8, 2017, pp. 081003–081003–13. doi:10.1115/1.4035662.

[29] Paliath, U., and Premasuthan, S., "Large Eddy Simulation for Jet Installation Effects," *19th AIAA/CEAS Aeroacoustics Conference*, 2013, pp. 1–10. doi:10.2514/6.2013-2137, URL http://arc.aiaa.org/doi/abs/10.2514/6.2013-2137.

[30] Langtry, R. B., Larssen, J. V., Winkler, C. M., Dorgan, a. J., and Mani, M., "DDES and Acoustic Prediction of Rudimentary Landing Gear Experiment Using Unstructured Finite Volume Methods," *Flow, Turbulence and Combustion*, Vol. 91, No. 3, 2013, pp. 717–745. doi:10.1007/s10494-013-9487-3, URL http://link.springer.com/10.1007/s10494-013-9487-3.

[31] Tyacke, J. C., Wang, Z.-N., and Tucker, P. G., "LES-RANS of installed ultra-high bypass-ratio coaxial jet aeroacoustics with a finite span wing-flap geometry and flight stream – Part 1: round nozzle," *23rd AIAA/CEAS Aeroacoustics Conference*, AIAA, Denver, Colorado, 2017. doi:10.2514/6.2017-3854.

[32] Shur, M. L., Spalart, P. R., and Strelets, M. K., "Noise prediction for increasingly complex jets . Part I : Methods and tests," *International Journal of Aeroacoustics*, Vol. 4, No. 3&4, 2005, pp. 213–246. doi:10.1260/1475472054771376.

[33] Naqavi, I. Z., Wang, Z.-N., and Tucker, P. G., "Far-field noise prediction for jets using Large-eddy simulation (LES) and Ffowcs Williams-Hawkings (FW-H) method," *International Journal of Aeroacoustics*, Vol. 15, No. 8, 2016, pp. 1–29. doi:10.1177/1475472X16672547.

[34] Rahier, G., Huet, M., and Prieur, J., "Additional terms for the use of Ffowcs Williams and Hawkings surface integrals in turbulent flows," *Computers and Fluids*, Vol. 120, 2015, pp. 158–172. doi:10.1016/j.compfluid.2015.07.014, URL http://dx.doi.org/10.1016/j.compfluid.2015.07.014.

[35] Pérez Arroyo, C., Daviller, G., Puigt, G., and Airiau, C., "Hydrodynamic - Acoustic Filtering of a Supersonic Under-expanded Jet," *ERCOFTAC workshop Direct and Large- Eddy Simulation 10*, 2015, pp. 1–6.

[36] Tyacke, J. C., Mahak, M., and Tucker, P. G., "Large-Scale Multifidelity, Multiphysics, Hybrid Reynolds-Averaged Navier–Stokes/Large-Eddy Simulation of an Installed Aeroengine," *Journal of Propulsion and Power*, Vol. 32, No. 4, 2016, pp. 997–1008. doi:10.2514/1.B35947, URL http://arc.aiaa.org/doi/10.2514/1.B35947.

[37] Mockett, C., Fuchs, M., Kramer, F., Michel, U., and Thiele, F., "Turbulence Modelling and Meshing Developments for the Prediction of Jet Noise Installation Effects," *22nd AIAA/CEAS Aeroacoustics Conference*, AIAA/CEAS, Lyon, 2016, p. 2933.

[38] Mahak, M., Naqavi, I. Z., and Tucker, P. G., "Cost-effective hybrid RANS-LES type method for jet turbulence and noise prediction," *International Journal of Aeroacoustics*, Vol. 16, No. 1-2, 2017, pp. 97–111. doi:10.1177/1475472X16684702.

[39] Jameson, A., "Formulation of Kinetic Energy Preserving Conservative Schemes for Gas Dynamics and Direct Numerical Simulation of One-Dimensional Viscous Compressible Flow in a Shock Tube Using Entropy and Kinetic Energy Preserving Schemes," *Journal of Scientific Computing*, Vol. 34, No. 2, 2007, pp. 188–208. doi:10.1007/s10915-007-9172-6.

[40] Eastwood, S., Tucker, P., Xia, H., Dunkley, P., and Carpenter, P., "Large-Eddy Simulations and Measurements of a Small-Scale High-Speed Coflowing Jet," *AIAA Journal*, Vol. 48, No. 5, 2010, pp. 963–974. doi:10.2514/1.44534, URL http://arc.aiaa.org/doi/abs/10.2514/1.44534.

[41] Xia, H., Tucker, P. G., and Eastwood, S., "Large-eddy simulations of chevron jet flows with noise predictions," *International Journal of Heat and Fluid Flow*, Vol. 30, No. 6, 2009, pp. 1067–1079. doi:10.1016/j.ijheatfluidflow.2009.05.002, URL http://dx.doi.org/10.1016/j.ijheatfluidflow.2009.05.002.

[42] Eastwood, S., Tucker, P., Xia, H., and Klostermeier, C., "Developing Large Eddy Simulation for Turbomachinery Applications," *Phil. Trans. R. Soc. A*, Vol. 367, No. 1899, 2009, pp. 2999–3013.

[43] Eastwood, S., "Hybrid LES – RANS of Complex Geometry Jets," Phd thesis, University of Cambridge, 2009.

[44] Spalart, P. R., and Allmaras, S. R., "A one-equation turbulence model for aerodynamic flows," *La Recherche Aérospatiale*, Vol. 1, No. 1, 1994, pp. 5–21. URL http://www.mendeley.com/research/a-oneequation-turbulence-model-for-aerodynamic-flows/.

[45] Liu, Y., Tucker, P. G., and Kerr, R. M., "Linear and nonlinear model large-eddy simulations of a plane jet," *Computers and Fluids*, Vol. 37, 2008, pp. 439–449. doi:10.1016/j.compfluid.2007.02.005.

[46] Smagorinsky, J., "General circulation experiments with the primitive equations. I. The basic experiment," *Monthly Weather Review*, Vol. 91, No. 3, 1963, pp. 99–165.

[47] Najafi-Yadzi, A., Bres, G. A., and Mongeau, L., "An acoustic analogy formulation for moving sources in uniformly moving media," *Proc. R. Soc. A*, 2010, pp. 1–22. doi:10.1098/rspa.2010.0172.

[48] Bridges, J., and Wernet, M. P., "Validating Large-Eddy Simulation for Jet Aeroacoustics," *Journal of Propulsion and Power*, Vol. 28, No. 2, 2012, pp. 226–234. doi:10.2514/1.B34385.

[49] Goldstein, M. E., "A generalized acoustic analogy," *Journal of Fluid Mechanics*, Vol. 488, 2003, pp. 315–333. doi:10.1017/S0022112003004890.

[50] Karabasov, S. A., Afsar, M. Z., Hynes, T. P., Dowling, A. P., McMullan, W. A., Pokora, C. D., Page, G. J., and McGuirk, J. J., "Jet Noise : Acoustic Analogy Informed by Large Eddy Simulation," *AIAA Journal*, Vol. 48, No. 7, 2010, pp. 1312–1325. doi:10.2514/1.44689.

[51] Deck, S., and Laraufie, R., "Numerical investigation of the flow dynamics past a three-element aerofoil," *J. Fluid Mech.*, Vol. 732, 2013, pp. 401–444. doi:10.1017/jfm.2013.363.

[52] Brown, C. A., "Jet-Surface Interaction Test : Far-Field Noise Results," *Journal of Engineering for Gas Turbines and Power*, Vol. 135, No. July, 2013, pp. 071201–1 – 071201–7. doi:10.1115/1.4023605.

[53] Mockett, C., Fuchs, M., Kramer, F., Michel, U., Thiele, F., and Steger, M., "Further Development and Initial Validation of Innovative DES-Based Approaches for the Prediction of Jet Noise Installation Effects," *ASME Turbo Expo*, 2017, p. V02CT43A013. 11 pages. doi:10.1115/GT2017-65253.

[54] Tyacke, J. C., Wang, Z.-N., and Tucker, P. G., "Noise source , length and time scale distributions in installed jets with a flight stream," *AIAA/CEAS Aeroacoustics Conference*, AIAA, Atlanta, Georgia, 2018, p. 11 pages. doi:10.2514/6.2018-3619.